Appendix 2

Luminescence analysis and dating of sediments from archaeological sites and valley fill sequences

Alan J. Cresswell, David C.W. Sanderson, Timothy C. Kinnaird & Charles French

A2.1. Summary

This report describes Optically Stimulated Luminescence (OSL) investigations to provide a temporal framework to underpin investigations into the early Holocene topography of the Ramla and Marsalforn valleys, Gozo, and excavations at the Neolithic temple sites of Ġgantija, Gozo and Skorba, Malta, and the Punic-Roman site of Tal-Istabal, Qormi, on the outskirts of Valletta in Malta. These chronologies are also of benefit in understanding the development and history of these World Heritage Site monuments.

Although the local limestone geology was not expected to generate quartz-rich sediments, micromorphology conducted by the *FRAGSUS* team had shown the presence of sand sized quartz within local soils and sediments. Field and laboratory profile measurements were conducted on 60 samples from seven sequences to provide initial assessments of the brightness of luminescence signals from different silicate fractions, and the stratigraphic relationships between the range of signals measured, to assess the prospects of being able to determine robust age quantifications from these materials, and guide the collection of larger tube samples for OSL dating. Laboratory profiling measurements confirmed the presence of quartz in prepared sediments with generally bright luminescence signals, and opening the way for Single Aliquot Regenerative (SAR) OSL dating of quartz fractions from 12 tube samples collected from five sites, with accompanying field and laboratory dose rate measurements.

At both the Ġgantija Temple (Gozo) and Skorba Temple/settlement (Malta), profile samples collected from below the modern agricultural soils show photon counts and apparent doses that increase steadily with depth, indicating that these buried soils accumulated gradually without subsequent disturbance. The OSL equivalent dose measurements showed no significant variation between aliquots, again indicating that the quartz minerals had been zeroed prior to deposition without subsequent disturbance, allowing robust ages to be determined. For both these locations, the OSL dates for the bottom of the sequences indicating the onset of soil accumulation were consistent at 8560±630 BC (Ġgantija) and 8780±710 BC (Skorba). At Ġgantija the top of this buried soil gives a Bronze Age OSL date of 1140±250 BC, whereas the OSL date for the top of the buried soil at Skorba is 7760±560 BC, predating the known Neolithic activity at the site.

At Ramla and Marsalforn Valleys, OSL investigations were conducted on sequences of buried palaeosols, hillwash and alluvial deposits. For Marsalforn Valley, the profile samples show a slight increase in photon counts and dose with depth, suggesting a gradual build-up of material. However, the OSL samples show evidence of multiple dose components, including high dose residuals, consistent with variations in light exposure during the reworking of soils. The upper sample could not be reliably dated, and the lower two samples generate the same age within uncertainties (1560±240 BC and 1480±340 BC). The Ramla Valley profiles are complex, showing relatively high photon counts in the upper samples decreasing with depth, and no clear trend in the apparent dose estimates. The OSL samples all show evidence of multiple dose components, including both high dose residuals and modern OSL dates in the nineteenth and early twentieth centuries AD.

The investigations reported here are the first applications of luminescence techniques on these sites. The results show that quartz OSL is an applicable approach to investigations of these sites, and that luminescence profiling techniques using field instruments and laboratory methods are highly informative. There is clearly the potential to apply these techniques to establish more detailed chronologies in future work.

A2.2. Introduction

Situated in the Mediterranean, the archipelago of Malta and Gozo lies close to the route of the spread of agricultural practices from the Fertile Crescent along the southern coast of Europe, and later dispersions of Neolithic cultural practices including monumental architecture. Agriculture based on wheat cultivation developed in the Fertile Crescent of the Near East around 9000 BC, and spread along the southern coast of Europe, largely associated with maritime movement, with early farming communities on Crete (*c.* 7000 BC), east-central Greece (*c.* 6500 BC), Dalmatia (*c.* 5700 BC), southern Italy (*c.* 6000 BC) and southern Iberia (*c.* 6000 BC). The first evidence of Holocene human activity on Malta, evidenced by pottery shards and the charred remains of fires and bones, has been dated to approximately 5000 BC (Trump 1966; Renfrew 1972). The emergence of visible social complexity is evidenced in enclosed sites and communal tombs in southeast Spain in the later fourth millennium BC. It has been suggested that the necessity of water control in arid regions lead, in part, to the emergence of such social complexity.

The archipelago of Malta and Gozo has a seasonally dry and hot climate which makes the natural landscape marginal for agriculture, and it has been presumed that from prehistoric times terracing has been extensively adopted to conserve soils and moisture, improving the landscape for agriculture (Sagona 2015). In addition, common to other parts of the Mediterranean, the islands are believed to have been prone to deforestation, drought and soil erosion since Neolithic times (Bevan & Conolly 2013; Brandt and Thornes 1996; Djamali *et al*. 2013; Grima 2008a; Grove & Rackham 2003; Hughes 2011). The research on these islands within the *FRAGSUS Project* aimed to examine these assumptions through a detailed geoarchaeological and micromorphological study of two significant Neolithic palaeosol contexts from beneath the Santa Verna and Ġgantija Neolithic temple sites and the associated Marsalforn and Ramla valleys to either side of the Xagħra plateau on Gozo.

The work reported here uses luminescence techniques to develop chronological frameworks for these investigations. Chronologies have previously been developed based on radiocarbon analysis (Trump 1966; Renfrew 1972) for the temple complex at Skorba with calibrated dates ranging from *c*. 5000 BC to 3200 BC, however luminescence approaches have not to date been widely used on Malta and Gozo. Luminescence techniques have, however, been widely used in Neolithic contexts in the Mediterranean, and beyond, for establishing robust chronologies. Examples in the Mediterranean region include megalithic tombs at Cabeço dos Pendentes in Portugal (Kinnaird *et al*. 2015), Neolithic monuments in Corsica (Sanderson *et al.* 2014), deltaic sediments associated with cultural activity from the Neolithic onwards on Crete (Zacharias *et al.* 2000), and Neolithic settlements, cemeteries and landscapes in Cyprus (Kinnaird *et al.* 2007, 2013). These techniques have also been used to investigate rates of soil erosion in Greece (Fuchs *et al.* 2004) using material largely devoid of quartz minerals, and river development in Crete (Macklin *et al.* 2010) where quartz minerals are derived from local sandstone.

The geology of Malta is dominated by limestone, resulting in locally derived soils largely devoid of silicate minerals suitable for luminescence dating. However, windblown sands from the Sahara are expected to deliver small quantities of silicates to the island. The Sahara is the largest source of aeolian dust, accounting for approximately half of the total atmospheric mineral dust burden (Scheuvens *et al.* 2013), with dust from the Sahara deposited in south and central America, the Atlantic Ocean, Europe and the Mediterranean, India and sub-Saharan Africa over the last 5 million years. In the Western Mediterranean, the dominant source of dust is from Tunisia and northern Algeria with dust generated from dry lakes and alluvial deposits (Scheuvens *et al*. 2013). Dust emission is a complex relationship between wind and surface conditions. Generally, small particles (<70 μm) experience large interparticle cohesive forces relative to aerodynamic forces acting on the particles, with aerodynamic forces becoming relatively larger with larger grain size. Thus, larger grains are mobilized first and follow ballistic curves with impacts on the ground mobilizing the smaller particles (Schepanski 2018). Alluvial sediments are very prone to wind erosion, with temporally varying erodibility as the most susceptible particles are removed from the sediment with refreshing of sediments during floods (Schepanski 2018). Thus, dust emission strongly reflects environmental conditions, being largest in dry periods. The transport distance strongly depends on residence time in the atmosphere; fine particles (<70 μm) are kept aloft by atmospheric turbulence for durations of weeks and can be transported thousands of km, with larger particles generally depositing within a day although larger particles are occasionally found >1000 km from their source (Schepanski 2018). The typical red Mediterranean soils, or *terra rossa*, on limestone substrates found throughout this region are also common on Malta and Gozo. The silicate minerals in similar soils in Greece have been attributed to aeolian deposition of material blown from North Africa (MacLeod 1980; Mizota *et al*. 1988), although larger mineral grains in low lying

regions have been attributed to local beaches (Mizota *et al.* 1988). Yaalon (1997) argues that aeolian dust from the Sahara contributes to all soils in the Mediterranean region, with up to 50 per cent of aeolian material in limestone derived soils. Micromorphological investigations conducted within the *FRAGSUS Project* have already shown the presence of sand sized silicates within local soils and sediments (French *et al.* 2018).

Quartz grains from the Sahara are expected to be well suited to OSL dating, with a reputation for being bright (e.g. Bevan *et al*. 2013; Kinnaird *et al.* 2013; Mauz *et al.* 2009; Russell & Armitage 2012), but may not be abundant. Fuchs *et al*. (2004) have shown that similar soils in Greece without abundant quartz can be accurately dated. The relative abundance of these grains may reflect climatic variations, in particular changes in aridity in the Sahara which may alter the supply of grains and prevailing wind directions and strengths affecting the transport of these grains to Malta. Although it is expected that aeolian grains will be bleached in transit, many of the grains in the soils will have been transported to the islands before incorporation in the soils having been reworked from earlier soils. The aim of the OSL investigations reported here is to provide a temporal framework to underpin investigations into the earlier Holocene topography of the Ramla and Marsalforn valleys, Gozo, and on the excavations at the Neolithic temple sites of Ġgantija, Gozo and Skorba, Malta. The objective of the field campaign was to retrieve samples from existing soil/sediment profiles in Gozo for OSL dating, and to sample the new test excavations at Skorba in Malta for micromorphology, physical characterization and OSL dating.

On Gozo, three sites were visited: the Neolithic temple site of Ġgantija on the Xagħra plateau; the Ramla valley, which separates the Xagħra plateau from the Nuffara plateau to the south; and the Marsalforn valley, a tributary valley of the Ramla. From the more extensive fieldwork of French and Taylor (see Chapter 5), it is known that the plateaus are largely denuded of soil and vegetation (i.e. Holocene strata), the little that remains in terms of (Holocene) hillwash (colluvium) and alluvial deposits is concentrated on the lower slopes and in the lower parts of the topography, such as in the Ramla and Marsalforn valleys. The OSL investigations in the Ramla and Marsalforn valleys were undertaken with the aim of generating a chronology for the sequences of buried palaeosols, hillwash and alluvial deposits preserved there, and thus the means to re-construct the earlier Holocene to Recent development of the Gozo valley-scale with time. At Ġgantija, the objective was to provide a chronology for the buried soil sequence located off-site, in Test Pit 1, to establish the soil catena history for this part of Gozo.

On Malta, two sites were visited: the Neolithic temple site of Skorba and a development site with Punic-Roman archaeology present at Marsa in Valletta. Test excavations in 2016 on the western edge of the Skorba temple/settlement had revealed a 1.5 m deep sequence, within which three curvilinear stone walls of the Neolithic period effectively sealed *c*. 70 cm of soil accumulation. From field excavations, it is suggested that the lower *c*. 50 cm of this soil was in fact a buried soil, albeit with the upper *c.* 20 cm probably being disturbed (in the past) (see Chapter 5). The objective here, was again to provide a chronology for the buried soil sequence, and identify any correlations between the soil formation/properties and prehistoric activity.

A2.3. Methods

A2.3.1. Sampling and field screening measurements

The aim of the April 2016 fieldwork was to retrieve samples from existing soil/sediment profiles in Gozo for OSL dating, and to sample the new test excavations at Skorba in Malta for OSL dating, physical characterization and micromorphology. In addition, a development site with Punic-Roman archaeology present at Marsa in Valletta was also sampled.

All samples were first appraised using the SUERC portable OSL reader, following an interleaved sequence of system dark count (background), infra-red stimulated luminescence (IRSL) and OSL, similar to that described by Sanderson and Murphy (2010). This method allows for the calculation of IRSL and OSL net signal intensities, depletion indices and IRSL:OSL ratios, which are then used to generate luminescence-depth profiles. The patterns in these data allow initial inferences and conjectures about trends or discontinuities in field profiles to be made, in combination with other initial observations of the sedimentology, which are used to refine further sampling. These can be refined and evaluated through further laboratory assessments.

A2.3.2. Laboratory calibrated screening measurements

Having established that there were measureable stratigraphic trends in the luminescence 'field' profiles, it remained to be determined whether these signal progressions are influenced, or indeed controlled, by sensitivity variations. Laboratory profiling provides one means to assess luminescence sensitivity distributions, and the first preliminary assessment of apparent doses.

All profiling samples were wet sieved at 90 and 250 μm. The 90–250 μm fractions were then subjected

to acid treatments of 1M HCl for 10 minutes, 15 per cent HF for 15 minutes and 1M HCl for 10 minutes. The samples were split into two fractions, one for polymineral analysis and one for quartz analysis. The quartz fraction was submitted to further acid treatments of 40 per cent HF for 40 minutes and 1M HCl for 10 minutes.

Luminescence sensitivities (Photon Counts per Gy) and stored doses (Gy) were evaluated from paired aliquots of the polymineral and HF-etched quartz fractions, using Risø DA-15 automatic readers (following procedures established in Burbidge *et al*. 2007; Sanderson *et al*. 2001, 2003). The readout cycles comprised a natural readout, followed by readout cycles for a nominal 1 Gy test dose, a 5 Gy regenerative dose, and a further 1 Gy test dose. For the polymineral samples, a 220°C preheat was followed by 60s OSL measurements using the IR LEDs at 50°C, the blue LEDs at 125°C, and a TL measurement to 500°C. For the quartz samples, a 220°C pre-heat was used with 60s OSL measurements using the blue LEDs.

A2.4. Quartz OSL SAR measurements

A2.4.1. Sample preparation

Water contents

Dating materials and bulk sediment samples were weighed, saturated with water and re-weighed. Following oven drying at 50 °C to constant weight, the actual and saturated water contents were determined as fractions of dry weight. These data were used, together with information on field conditions to determine water contents and an associated water content uncertainty for use in dose rate determination.

HRGS and TSBC sample preparation

Bulk quantities of material, weighing 50–100 g, were removed from each full dating and bulk sediment sample for environmental dose rate determinations. These dried materials were transferred to high-density-polyethylene (HDPE) pots and sealed with epoxy resin for high-resolution gamma spectrometry (HRGS). Each pot was stored for three weeks prior to measurement to allow equilibration of ^{222}Rn daughters. A further 20 g of the dried material was used in thick source beta counting (TSBC; Sanderson 1988).

Quartz mineral preparation

Approximately 5–10 g of material was removed for each tube and processed to obtain sand-sized quartz grains for luminescence measurements. Each sample was wet sieved to obtain the 90–150 and 150–250 μm fractions. The 90–150 μm fractions were treated with 1 M hydrochloric acid (HCl) for 10 minutes, 15 per cent hydrofluoric acid (HF) for 15 minutes, and 1 M HCl for a further 10 minutes. The HF-etched sub-samples were then centrifuged in sodium polytungstate solutions of ~2.58, 2.62, and 2.74 g cm^{-3}, to obtain concentrates of potassium-rich feldspars (<2.58 g cm^{-3}), sodium feldspars (2.58–2.62 g cm^{-3}) and quartz plus plagioclase (2.62–2.74 g cm^{-3}). The selected quartz fraction was then subjected to further HF and HCl washes (40 per cent HF for 40 minutes, followed by 1M HCl for 10 minutes).

All materials were dried at 50° C and transferred to Eppendorf tubes. The 40 per cent HF-etched, 2.62–2.74 g cm^{-3} 'quartz' 90–150 μm fractions were dispensed to 10 mm stainless steel discs for measurement. The purity of which was checked using a Hitachi S-3400N scanning electron microscope (SEM), coupled with an Oxfords Instruments INCA EDX system, to determine approximate elemental concentrations for each sample. 8–32 aliquots were dispensed for each sample, depending on quartz yield.

A2.4.2. Measurements and determinations

Dose rates

Dose rates were measured in the laboratory using HRGS and TSBC. Full sets of laboratory dose rate determinations were made for all samples.

HRGS measurements were performed using a 50 per cent relative efficiency 'n' type hyper-pure Ge detector (EG&G Ortec Gamma-X) operated in a low background lead shield with a copper liner. Gamma ray spectra were recorded over the 30 keV to 3 MeV range from each sample, interleaved with background measurements and measurements from SUERC Shap Granite standard in the same geometries. Sample counts were for 80 ks. The spectra were analysed to determine count rates from the major line emissions from ^{40}K (1461 keV), and from selected nuclides in the U decay series (^{234}Th, ^{226}Ra + ^{235}U, ^{214}Pb, ^{214}Bi and ^{210}Pb) and the Th decay series (^{228}Ac, ^{212}Pb, ^{208}Tl) and their statistical counting uncertainties. Net rates and activity concentrations for each of these nuclides were determined relative to Shap Granite by weighted combination of the individual lines for each nuclide. The internal consistency of nuclide specific estimates for U and Th decay series nuclides was assessed relative to measurement precision, and weighted combinations used to estimate mean activity concentrations (Bq kg^{-1}) and elemental concentrations (per cent K and ppm U, Th) for the parent activity. These data were used to determine infinite matrix dose rates for alpha, beta and gamma radiation.

Beta dose rates were also measured directly using the SUERC TSBC system (Sanderson 1988). Count rates were determined with six replicate 600 s counts on

each sample, bracketed by background measurements and sensitivity determinations using the Shap Granite secondary reference material. Infinite-matrix dose rates were calculated by scaling the net count rates of samples and reference material to the working beta dose rate of the Shap Granite (6.25 ± 0.03 mGy a^{-1}). The estimated errors combine counting statistics, observed variance and the uncertainty on the reference value.

The dose rate measurements were used in combination with the assumed burial water contents, to determine the overall effective dose rates for age estimation. Cosmic dose rates were evaluated by combining latitude and altitude specific dose rates (0.17 ± 0.01 mGy a^{-1}) for the site with corrections for estimated depth of overburden using the method of Prescott and Hutton (1994).

Quartz SAR luminescence measurements

All measurements were conducted using a Risø DA-15 automatic reader equipped with a $^{90}Sr/^{90}Y$ β-source for irradiation, blue LEDs emitting around 470 nm and infrared (laser) diodes emitting around 830 nm for optical stimulation, and a U340 detection filter pack to detect in the region 270–380 nm, while cutting out stimulating light (Bøtter-Jensen *et al*. 2000).

Equivalent dose determinations were made on sets of 8–32 aliquots per sample, using a single aliquot regeneration (SAR) sequence (cf. Murray & Wintle 2000). Using this procedure, the OSL signal levels from each individual disc were calibrated to provide an absorbed dose estimate (the equivalent dose) using an interpolated dose-response curve, constructed by regenerating OSL signals by beta irradiation in the laboratory. Sensitivity changes which may occur as a result of readout, irradiation and preheating (to remove unstable radiation-induced signals) were monitored using small test doses after each regenerative dose. Each measurement was standardized to the test dose response determined immediately after its readout, to compensate for changes in sensitivity during the laboratory measurement sequence. The regenerative doses were chosen to encompass the likely value of the equivalent (natural) dose. A repeat dose point was included to check the ability of the SAR procedure to correct for laboratory-induced sensitivity changes (the 'recycling test'), a zero dose point is included late in the sequence to check for thermally induced charge transfer during the irradiation and preheating cycle (the 'zero cycle'), and an IR response check included to assess the magnitude of non-quartz signals. Regenerative dose response curves were constructed using doses of 0.5, 1, 2.5, 10 and 2.5 Gy, with test doses of 1.5 Gy. The 32 aliquot sets were sub-divided into eight subsets of four aliquots, such that eight preheating regimes were explored (200° to 270° C, in 10° C increments), the small aliquot sets were divided into a small number of sub-sets.

A2.5. Results

A2.5.1. Sampling and preliminary luminescence stratigraphies

Field work was conducted in April 2016, with the collection of seven profiles and 12 OSL dating samples, as summarized in Tables A2.1 and A2.2, with selected photographs of the sampling sites in Figures A2.1 to A2.8. Field gamma spectrometry measurements were also collected for each of the OSL sampling sites, reported in Table A2.4. All samples were first appraised using the SUERC portable OSL reader, to produce IRSL and OSL net signal intensities, depletion indices and IRSL:OSL ratios, and luminescence-depth profiles. The results are shown in Figures A2.9 to A2.13, and presented in the Table A2.1.

A2.5.2. Gozo

Three profiles were sampled on Gozo:

Profile 1: an erosion cut profile in the middle Marsalforn valley, opposite Ta'Manea in Weid ir-Rigu (profile BH110; N 36 03.472/ E 014 14.946) was cut back and sampled for OSL. This profile comprised *c*. 3.7 m of rubbly fine sandy/silt loam which was interrupted by two incipient buried soil horizons at *c*. 1.75–2.10 and 2.70–2.85 m down-profile. Figures A2.1 and A2.2 show photographs of this site. A series of 10 small bulk samples were taken for luminescence profiling from 1.75–3.25 m. Initial field impressions, including the luminescence profiles (Fig. A2.9) showing broadly similar luminescence intensities within and between the soils with the exception of P1/2, were that this represents an age-related gradual accumulation of hillwash-type sediment throughout the profile. Three OSL tube samples at 1.75, 2.65 and 3.2 m down-profile were collected (as indicated in Fig. A2.9), representing the top of the upper buried soil and the top and bottom of the lower soil.

Profile 2: an erosion cut profile in the lower Ramla valley about 200 m inland from Ramla Bay (profile BH 66; N 36 03.442/E 014 17.045) was cut back and sampled for OSL. This profile is comprised of a series of alternating horizons of calcitic silt loam and coarse sand/pebble horizons, with the whole profile generally fining upwards, over a depth of *c*. 1.4 m. The site is shown in Figure A2.3. A series of 11 small bulk samples were taken from the finer silt loam horizons for profiling (Fig. A2.10). These indicate that parts of the sedimentary sequence are likely to have been re-deposited without the luminescence signals being

Table A2.1. *Sample descriptions, contexts and archaeological significance of the profiling samples used for initial screening and laboratory characterization (estimated from local datums).*

	Field no.	SUTL no.	Depth /cm	Field description/ context	Archaeological significance
Ta'Manea, Marsalforn valley, Gozo off-site palaeoenvironmental proxy record; reconstruct earlier Holocene landscape of Gozo					
Profile 1	P1/1	2916A	180	above soil; pale yellowish-grey silty clay loam; hillwash	TAQ for age of buried soil (upper horizon)
	P1/2	2916B	195	buried old land surface/incipient soil in hillwash; pale yellowish brown silty clay loam with columnar ped structure	Buried soil surface 1.75–2.10 m (upper horizon)
	P1/3	2916C	205		
	P1/4	2916D	215	rounded limestone pebbles (<5 cm); erosion event/ temporary stream	TPQ for age of buried soil (upper horizon)
	P1/5	2916E	225	mix of greyish brown fine-medium sand and silt with limestone gravel pebbles	-
	P1/6	2916F	270		TAQ for age of buried soil (lower horizon)
	P1/7	2916G	290	buried old land surface/incipient soil in hillwash; pale yellowish brown fine sandy/silt loam with columnar blocky ped structure	Buried soil surface 2.70–2.85 m (lower horizon)
	P1/8	2916H	300		TPQ for age of buried soil (lower horizon)
	P1/9	2916I	310		-
	P1/10	2916J	320	pale grey silty clay loam with abundant rounded stone pebbles (<10 cm)	-
Ramla valley, Gozo exploited in the sixteenth and nineteenth centuries, with two superimposed systems of field and property boundaries; significance of profile – response to intensification of landscape/arable development on adjacent slopes					
Profile 2	P2/1	2920A	7.5	pale grey calcitic silt loam; calcitic alluvial lens	temporal constraints on degradation of upper slope
	P2/2	2920B	15		
	P2/3	2920C	27.5	fine pebbles (<2 cm); pebbly hillwash lens	fluvial phase
	P2/4	2920D	45	pale grey calcitic silt loam; calcitic alluvial lens	temporal constraints on degradation of upper slope
	P2/5	2920E	60		
	P2/6	2920F	75		
	P2/7	2920G	82.5		
	P2/8	2920H	105	fine sandy/silt loam	
	P2/9	2920I	115		Thin hillwash accumulations – may indicate some degree of balance and resilience in the landscape, or individual events removed most of the eroded soils to the sea
	P2/10	2920J	125		
	P2/11	2920K	140	weathered Globigerina bedrock	
Ġgantija Temple Test Pit 1, Gozo					
Profile 3	P3/1	2913A	10	greyish brown silt loam with common limestone fragments (<5 cm); Ap and terrace soil	-
	P3/2	2913B	18		later prehistoric and historic agricultural activity
	P3/3	2913C	25		
	P3/4	2913D	34	greyish brown silt loam with abundant limestone rubble and abundant Neolithic artefacts (pot, bone, lithics)	
	P3/5	2913E	45		
	P3/6	2913F	54		
	P3/7	2913G	68		Base of agricultural soil
	P3/8	2913H	78	brown silt loam with abundant Neolithic artefacts; *in situ* Ah of palaeosol	'field' profile implies some chronology with depth; beginnings of soil change associated with use and degradation of this landscape prior to construction of temple?
	P3/9	2913I	85	mid-brown silt loam with abundant Neolithic artefacts; buried lower A-B horizon of palaeosol	
	P3/10	2913J	92		Base of buried soil; constrain onset of soil accumulation

Table A2.1 *(cont.).*

	Field no.	SUTL no.	Depth /cm	Field description/ context	Archaeological significance
Skorba Neolithic site (Malta), Trench A, East section profiles 4 (East), 6 and 7 (south) taken on western edge of Skorba temple/settlement; like at Ġgantija, profiles encompass a buried soil associated with the landscape prior to construction of temple; here, sealed by three curvilinear stone walls					
Profile 4	P4/1	2924A	22	modern topsoil and fill of wall robber trench	-
	P4/2	2924B	32		-
	P4/3	2924C	41	dark brown sandy silt loam with occasional limestone rubble (<5 cm)	context [2]; fill of robber trench; re-deposited materials, carry residuals from earlier depositional cycle
	P4/4	2924D	51		
	P4/5	2924E	63	mix of dark brown sandy silt loam and limestone rubble (<15 cm)	context [11]; clear signal-depth progression through contexts 11, 20, 24
	P4/6	2924F	75		
	P4/7	2924G	86	dark greyish brown sandy silt loam; ?aggraded soil?	context [20]; aggraded soil?; later prehistoric and historic agricultural activity (as at Ġgantija?)
	P4/8	2924H	96		
	P4/9	2924I	106	dark brown sandy silt loam; disturbed, possible A horizon of palaeosol	context [24]; possible A horizon to buried soil; beginnings of soil change associated with use and degradation of this landscape prior to construction of temple?
	P4/10	2924J	113		
	P4/11	2924K	121	dark brown sandy silt loam; *in situ* B horizon of palaeosol	context [28]; in situ B horizon to buried soil
	P4/12	2924L	131		
	P4/13	2924M	138		potentially disturbed in prehistory; note inflection in luminescence intensities at *c*. 138 cm depth
	P4/14	2924N	147		
	P4/15	2924O	148		
Marsa, Valletta, Malta a Punic-Roman area of terraces and irrigation features; little in way of soil preservation due to commercial development at site					
Profile 5	P5/1	2929A	283	brown, calcitic, fine sandy/silt loam; ?pre-terrace soil/?palaeosol	TPQ for wall; sixteenth century AD soil accumulation and later terrace build-up?
	P5/2	2929B	287		
	P5/3	2929C	292		
	P5/4	2929D	298		
Skorba Neolithic site (Malta), Trench A, South section					
Profile 6	P6/1	2928A	65	dark brown fine sandy loam	context [23]
	P6/2	2928B	80	dark brown fine sandy loam; ?aggraded soil?	beneath context [26] – a possible Neolithic floor 75–78 cm; there is no clear progression in luminescence signals across the possible Neolithic floor/surface (in the position of this profile); this may indicate that this surface was not exposed for any length of time
	P6/3	2928C	90		
	P6/4	2928D	100	dark brown fine sandy loam with 20–25% small limestone rubble <5 cm); ?disturbed upper part of a palaeosol?	disturbed upper part of buried soil; reset during laying of floor / construction of Skorba complex?
	P6/5	2928E	115	dark brown fine sandy loam; *in situ* palaeosol	in situ buried soil; constrain onset of soil accumulation
	P6/6	2928F	120		
Skorba Neolithic site (Malta), Trump Trench cut in 1961					
Profile 7	P7/1	2931A	103	modern topsoil and fill of wall robber trench	within backfill to Trump's 1961 excavation; compare and contrast signal intensities with profiles 4 and 6
	P7/2	2931B	113		
	P7/3	2931C	123		
	P7/5	2931D	146	dark greyish brown sandy silt loam; ?aggraded soil?	should be equivalent to context [20] – samples P4/7 – 4/8

Table A2.2. *Sample descriptions, contexts and archaeological significance of sediment samples SUTL2914–2930 (†depths estimated relative to the overlying landforms for cosmic attenuation estimation).*

Sample ID	Profile	SUTL no.	Depth /cm	Description	Archaeological significance
OSL1	1	2917	175–180	=P1/1	Constrain final period soil was exposed, phase 2
OSL2	1	2918	265–270	=P1/6	Constrain final period soil was exposed, phase 1
OSL3	1	2919	320–330	= P1/10	Constrain onset of soil accumulation, phase 1
OSL4	2	2921	15–20	=P2/2	Provide a temporal constraint on degradation of upper slope
OSL5	2	2922	62–66	=P2/5	Provide temporal constraints on periods of colluviation
OSL6	2	2923	103–106	=P2/8	
OSL7	3	2914	78	=P3/8; buried soil 'A' horizon	Constrain final period soil was exposed
OSL8	3	2915	92	=P3/10; buried soil 'B' horizon	Constrain onset of soil accumulation
OSL9	5	2930	295–298	=P5/3 – 5/4	Constrain onset of soil accumulation, and date standing wall overlaying soil
OSL10	4	2925	118	=P4/11; [28]; rich-brown silty loam; 5% clay; 15–20% sand	Constrain final period soil was exposed
OSL11	4	2926	128	=P4/13	Provide temporal constraint on age of buried palaeo-surface
OSL12	4	2927	145	=P4/15	Constrain onset of soil accumulation

re-set at deposition; note, the step-like shifts in signal intensities at 46 cm and 115 cm. The most promising targets for dating are the horizons immediately beneath these units. Moreover, the ratio of net signal intensities between the upper (those not affected by recent soil turnover) and lower units, implies that the temporal range represented by these units may be relatively short. Three tube samples were taken for OSL dating at 15, 62 and 103 cm down-profile. The latter sample loci were also sampled for micromorphological analysis. Initial field impressions were not that clear, but the profile exhibited aggradation over time with at least two clear breaks, suggesting palaeo-surfaces of some kind at *c*. 46 cm and 115 cm, potentially indicative of changes in erosion processes from alternating fast/slow to a much slower aggradational dynamic.

Profile 3: Test Pit 1 which was excavated in 2014 on the western edge of the platform south of Ġgantija temple was re-excavated to reveal the complete profile through the agricultural soil build-up over the *in situ* buried soil. This is shown in Figure A2.4. A series of 10 small bulk samples were taken at approximately 10 cm intervals down-profile for luminescence profiling. Initial field impressions were that the agricultural soil had accumulated gradually over time, with a clear stratigraphic break at ~70 cm with the buried soil below, but with the buried soil exhibiting a longer and more stable time-depth. The luminescence profiles

Figure A2.1. *Marsalforn valley, Gozo.*

Figure A2.2. *Marsalforn valley, Gozo.*

Figure A2.3. *Ramla valley, Gozo.*

Figure A2.4. *Ġgantija Test Pit 1, Gozo.*

Figure A2.5. *(above) Skorba Neolithic site; trench A, East section; (left) trench A, South section, arrow shows position of Figure A2.6.*

Figure A2.6. *Skorba, Trench A, South section.*

(Fig. A2.11) show a significant increase in net signal below this horizon increasing with depth. Two tube samples for OSL dating were taken from the base of the agricultural soil (at 68 cm down-profile) and the base of the buried soil (at 92 cm down-profile).

A2.5.3. Skorba

The test excavations on the western edge of the Skorba temple/settlement revealed a 1.5 m deep sequence, within which three curvilinear stone walls of the Neolithic period effectively sealed *c.* 70 cm of soil accumulation. From field observation, it is suggested that the lower *c.* 50 cm of this soil was in fact a buried soil, albeit with the upper *c.* 20 cm probably having been disturbed (in the past). This soil exhibits a very fine sandy/silt dominated texture, which is very different from the soils present in the immediately surrounding area (in BH 618–625) which are much more dark brown, clay-rich, fine sandy/silty clay loams. Figures A2.5 and A2.6 show photographs of this site.

OSL profiling and sampling was undertaken at two profiles in the 2016 Trench A test excavation, from the east and south section faces. From the east section, 15 small bulk samples were taken at about 10 cm intervals from *c.* 22–148 cm down-profile (Profile 4) In the south section, 6 small bulk samples were taken between 65 and 120 cm down-profile, again to target the buried soil and soil accumulation above and the possible Neolithic floor/surface between 75 and 78 cm down-profile (Profile 6). The luminescence-depth profiles (Fig. A2.12) were extremely informative (profile 4):

1. unit [2] contains re-deposited materials, that carry luminescence residuals from an earlier depositional cycle;
2. units [11], [20] and [24] show a progression in luminescence signals with depth, consistent with a normal age-depth progression and a gradual accumulation of sediment; moreover, the range in signal intensities through these units is consistent with an age progression over a temporal range of a multiple of 1.5–2;
3. the upper *c.* 20 cm of the buried soil was probably disturbed in prehistoric times; note, the inflexion in luminescence intensities at *c.* 138 cm, indicating modification of this unit at the time this soil represented a former land-surface (and thus, that it is material at this depth, which should provide a constraint on the age of this palaeo-surface);
4. there is a clear temporal break between deposition of the soil, and units [24], [20] and [11]; this temporal break represents a short interval, equivalent to a temporal range in the order of 1.2–1.5; (profile 6)
5. there is no clear progression in luminescence signals across the possible Neolithic floor/surface (in the position of this profile); this may indicate that this surface was not exposed for any length of time (further characterization of these units in the laboratory will test this hypothesis); and
6. again, the upper part of the buried soil shows signs of disturbance in the past; note, by now the obvious inflexion in luminescence intensities occurs at *c.* 115 cm.

Three OSL tube samples were taken at 118, 128 and 145 cm down-profile from the east section, to target the chronology of the buried soil and old land surface. In both cases, the buried soil/soil accumulation/floor zone was also sampled for micromorphological analysis as well as physical characterization and geo-chemical analysis.

A2.5.4. Tal-Istabal, Qormi

Dr Tony Pace and Nathaniel Cutajar accompanied us to a commercial development site in Qormi on the northwestern side of a former marine embayment where a large Punic-Roman area of terraces and irrigation features had been recently excavated. Although there was little in the way of soil survival on this site due to total excavation, one zone of better preservation was located on the western edge of the site (N 36 03.423/E 014 17.047). Here beneath *c.* 2.7 m of surviving Globigerina Limestone terrace wall construction was *c.* 30–40 cm of agricultural/buried soil survival (Figs. A2.7 & A2.8). This was sampled for micromorphological analysis as well as physical characterization and geo-chemical analysis, and OSL profiling (Profile 5), with laser scans made of large sections of the terrace walls, and cut irrigation and burial features (by J. Bennett). The luminescence profile (Fig. A2.13) shows an increasing net signal with depth. A single tube sample was taken for OSL dating from the base of this profile.

A2.6. Laboratory calibrated screening measurements

The laboratory screening data are shown in Figures A2.14 to A2.20, with the data tabulated in the Supplement A Tables SA.2–SA.5. In most cases, the IRSL sensitivity is significantly lower than the OSL sensitivity. IRSL and OSL apparent doses follow similar stratigraphic trends, with a general increase in apparent dose with increasing depth for all profiles, for the sections at Marsalforn, Ġgantija (Gozo) and Skorba (Malta) the two estimates are in good agreement with agreement to within a factor of two to three for the other sections.

Figure A2.7. *Tal-Istabal, Qormi, Malta.*

Figure A2.8. *Tal-Istabal, Qormi, Malta.*

For Profile 1 (Fig. A2.14) there is a gradual increase in apparent dose with depth, for both IRSL and OSL which are in good agreement, with P1/4 showing higher apparent doses than the neighbouring samples, and a slight inversion of the profile with smaller apparent doses for the bottom two samples. OSL sensitivity is approximately two orders of magnitude greater than IRSL sensitivity, with both sensitivities showing a slight increase down the top half of the profile, a slight decrease down the bottom half, and a higher sensitivity for the sample below the soil layer. This broadly explains the variation of intensities observed in the field profiles (Fig. A2.9), and supports the conclusion that this profile represents a gradual accumulation of sediment.

For Profile 2 (Fig. A2.15) the sensitivities of both OSL and IRSL are similar and generally unchanged down the profile. The apparent dose in the IRSL measurements is approximately twice that of the OSL, with values for both scattered without any obvious trend down profile. For the lower part of the profile, this pattern reflects the field profile measurements (Fig. A2.10) which showed approximately constant intensities for most of the profile. However, the larger intensities for the uppermost three samples in the field measurements are not explained by the laboratory measurements. The approximately constant apparent doses and intensities suggest that the material in this profile accumulated rapidly.

For Profile 3 (Fig. A2.16) the apparent dose measured by OSL and IRSL is in general agreement, with no apparent trend down profile for the top 60 cm and a rapid increase with depth below that. The OSL sensitivities are two to three orders of magnitude greater than the IRSL sensitivities, with neither showing any significant trend down profile. This broadly reflects the field profiles (Fig. A2.11), which showed approximately constant and relatively low net intensities for the top 60 cm increasing significantly below that. Both field and laboratory measurements suggest a slow accumulation of material in the lower part of the profile, with a rapid accumulation for the top 60 cm.

For Profiles 4 and 6 (Figs. A2.17 & A2.19) the apparent dose increases gradually with depth down profile, with the OSL measurements generally slightly greater than the IRSL for profile 4. The OSL sensitivities are two to three orders of magnitude greater than the IRSL, without any obvious trend down profile with the exception of a significant reduction in sensitivity for P6/6. This reflects the observed gradual increase in net intensities down profile observed in the field profiles (Fig. A2.12), supporting the suggestion that

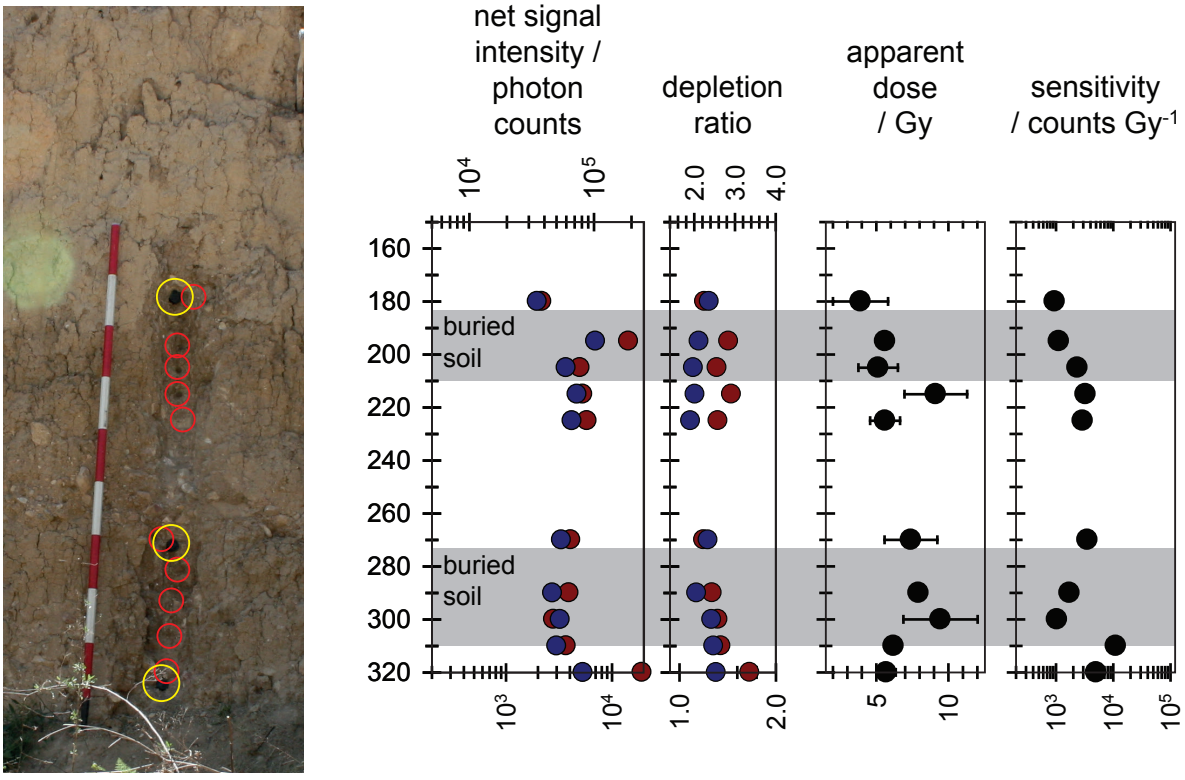

Figure A2.9. *Photograph, showing locations of profile sample (red circles) and OSL tubes (yellow circles), and luminescence-depth profile, for the sediment stratigraphy sampled in profile 1.*

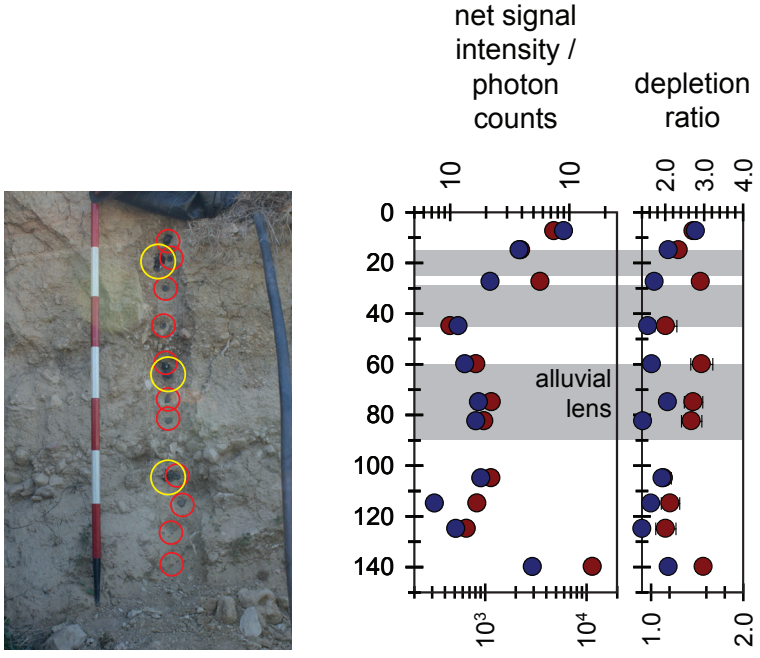

Figure A2.10. *Photograph, and luminescence-depth profile, for the sediment stratigraphy sampled in profile 3.*

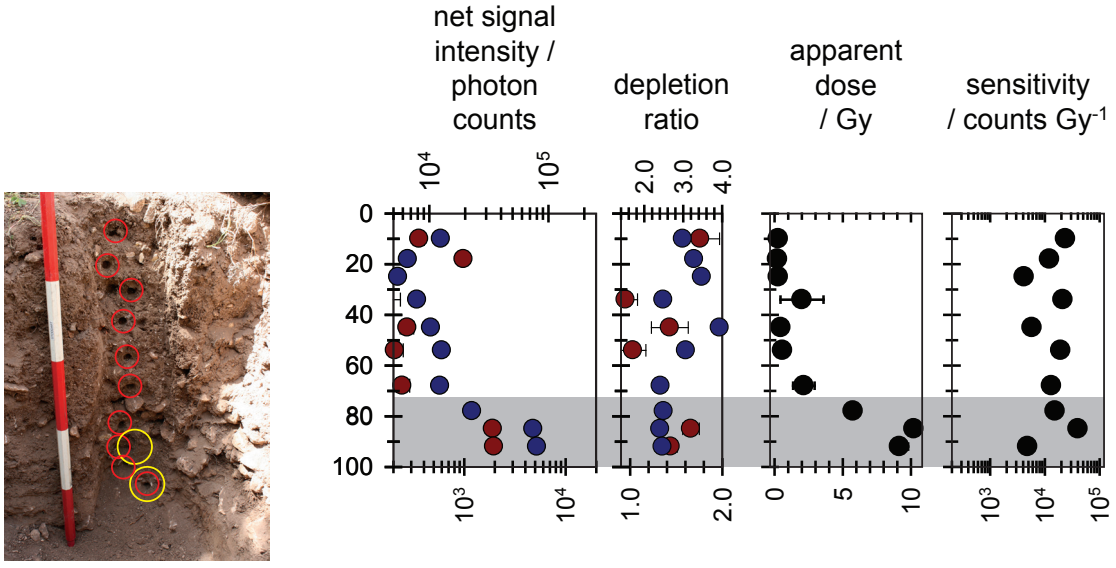

Figure A2.11. *Photograph, and luminescence-depth profile, for the sediment stratigraphy sampled in profile 2.*

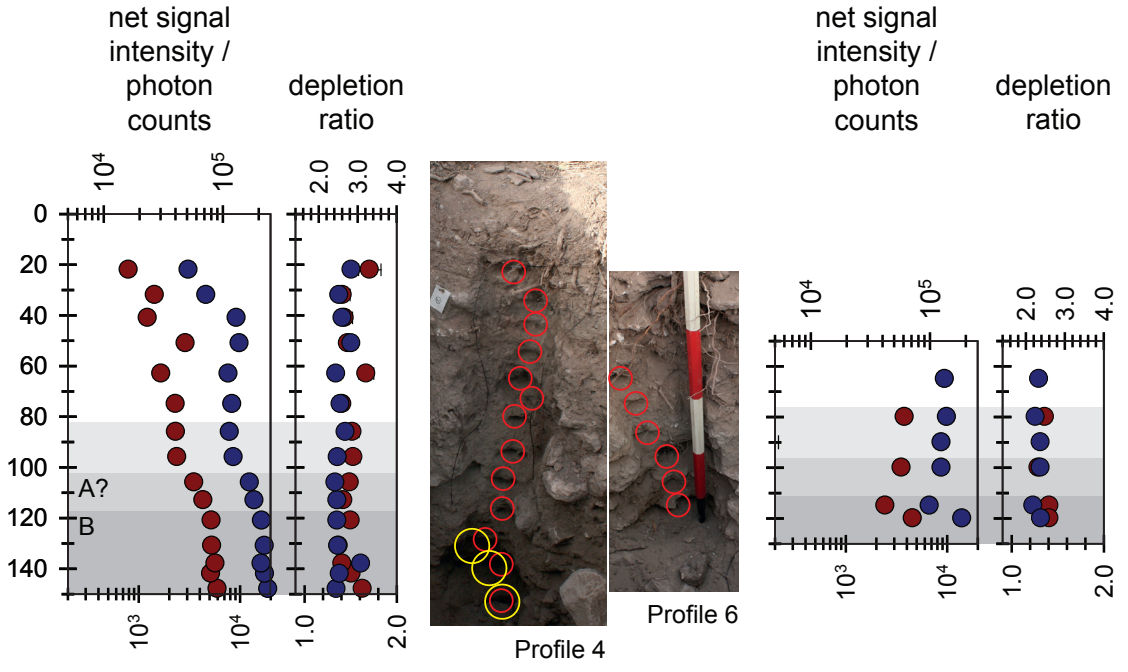

Figure A2.12. *Photograph, and luminescence-depth profile, for the sediment stratigraphy sampled in profiles 4 and 6.*

this represents a gradual accumulation of material over an extended period of time. The bottom sample of Profile 7 (Fig. A2.20) has similar apparent doses and sensitivities to the samples in profiles 4 and 6 that are identified as the same context, the upper samples within the backfill of the 1961 trench show a lower apparent dose and an inverted profile.

For Profile 5 (Fig. A2.18) the apparent dose measured by IRSL is 2–3 times that measured by OSL, with both increasing marginally down profile. The sensitivities for the two methods are similar, with differences less than an order of magnitude. This reflects the field profiles (Fig. A2.13) which showed a small increase in net intensities down profile.

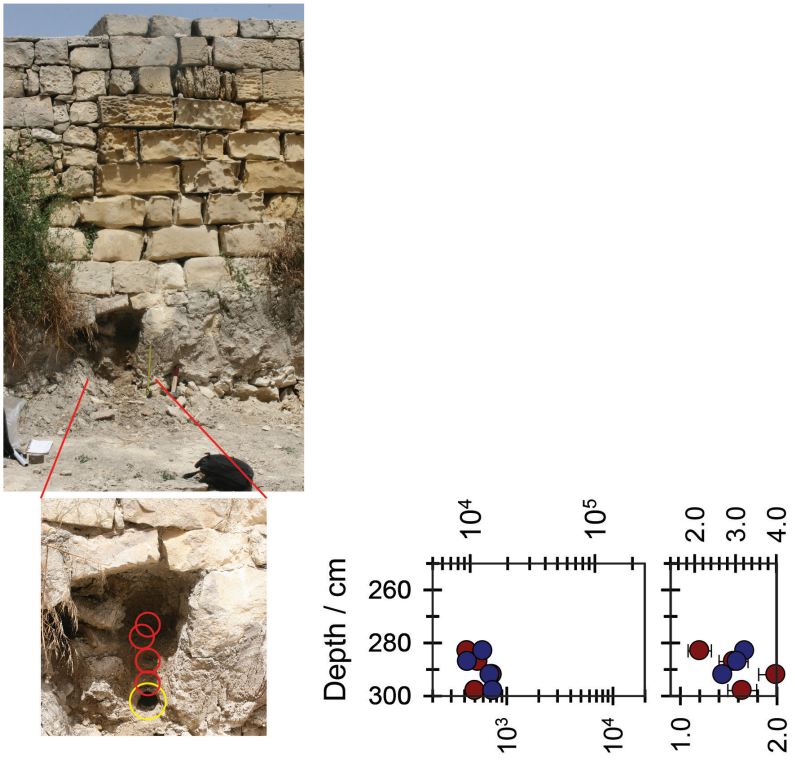

Figure A2.13. *Photograph, and luminescence-depth profile, for the sediment stratigraphy sampled in profile 5.*

A2.6.1. Dose rates

HRGS results are shown in Table A2.3, both as activity concentrations (i.e. disintegrations per second per kilogram) and as equivalent parent element concentrations (in per cent and ppm), based in the case of U and Th on combining nuclide specific data assuming decay series equilibrium.

Infinite matrix alpha, beta and gamma dose rates from HRGS are listed for all samples in Table A2.4, together with infinite matrix beta dose rates from TSBC and field gamma dose rates from FGS. Beta dose rates from HRGS are typically lower than those determined from TSBC by approximately 20 per cent. Wet gamma dose rates were measured in situ by FGS for each of the dating positions, and are typically lower than the HGRS gamma dose rates after water content corrections.

The water content measurements are given in Table A2.5, together with the assumed values for the average water content during burial. Field (ranging from 3–26 per cent of dry weight) and saturated (18–38 per cent of dry weight) water contents were determined from all samples in the laboratory, with working values for each site adopted for effective dose rate evaluation. Effective dose rates to the HF-etched 90–150 μm quartz grains are given in Table A2.5 (the mean of the TSBC and HRGS data, accounting for water content and grain size), together with the estimate of the gamma dose rate (the mean of the FGS and HRGS data, accounting for water content).

A2.6.2. Quartz single aliquot equivalent dose determinations

For equivalent dose determination, data from single aliquot regenerative dose measurements were analysed using the Risø TL/OSL Viewer programme to export integrated summary files that were analysed in MS Excel and SigmaPlot. The quality parameters for these analyses (sensitivity and sensitivity change, recycling ratio and response to zero dose) are given in Table A2.6. This shows considerable variation in sensitivity between samples, a small increase (5–15 per cent) in sensitivity for all samples, with all samples showing recycling ratios consistent with unity (with the exception of SUTL2923) and very low signals from the zero cycle and IRSL.

Composite dose response curves were constructed from selected discs and when possible, for each of the eight preheating groups from each sample, and used to estimate equivalent dose values for each individual

Table A2.3. *Activity and equivalent concentrations of K, U and Th determined by HRGS ([a]Shap granite reference, working values determined by David Sanderson in 1986, based on HRGS relative to CANMET and NBL standards; [b]Activity and equivalent concentrations for U, Th and K determined by HRGS (Conversion factors based on NEA (2000) decay constants): 40K: 309.3 Bq kg^{-1} %K^{-1}, 238U: 12.35 Bq kg^{-1} ppmU^{-1}, 232Th: 4.057 Bq kg^{-1} ppm Th^{-}).*

	Activity Concentration[a] / Bq kg^{-1}			Equivalent Concentration[b]		
SUTL no.	K	U	Th	K / %	U / ppm	Th / ppm
2914	264 ± 13	26.4 ± 1.6	26.6 ± 1.8	0.85 ± 0.04	2.14 ± 0.13	6.56 ± 0.45
(bulk)	260 ± 9	31.4 ± 1.2	25.2 ± 0.9	0.84 ± 0.03	2.54 ± 0.10	6.20 ± 0.22
2915	245 ± 9	19.9 ± 1.1	20.1 ± 0.9	0.79 ± 0.03	1.61 ± 0.09	4.95 ± 0.21
2917	294 ± 10	41.0 ± 1.5	24.2 ± 0.9	0.95 ± 0.03	3.32 ± 0.12	5.96 ± 0.22
(bulk)	225 ± 9	49.5 ± 1.6	22.0 ± 0.9	0.73 ± 0.03	4.01 ± 0.13	5.43 ± 0.22
2918	313 ± 9	42.1 ± 1.5	27.0 ± 0.9	1.01 ± 0.03	3.41 ± 0.12	6.65 ± 0.22
(bulk)	289 ± 9	61.3 ± 1.9	25.5 ± 0.9	0.93 ± 0.03	4.97 ± 0.15	6.28 ± 0.23
2919	240 ± 8	66.4 ± 1.9	20.8 ± 0.9	0.78 ± 0.03	5.37 ± 0.16	5.13 ± 0.22
(bulk)	268 ± 9	77.8 ± 2.2	25.0 ± 0.9	0.87 ± 0.03	6.30 ± 0.18	6.17 ± 0.23
2921	173 ± 7	31.4 ± 1.3	17.8 ± 0.8	0.56 ± 0.02	2.55 ± 0.10	4.38 ± 0.20
2922	164 ± 8	34.1 ± 1.3	17.4 ± 0.9	0.53 ± 0.02	2.76 ± 0.11	4.28 ± 0.21
2923	140 ± 9	42.0 ± 1.5	17.3 ± 0.9	0.45 ± 0.03	3.41 ± 0.12	4.25 ± 0.22
(bulk)	228 ± 10	41.5 ± 1.6	18.8 ± 0.9	0.74 ± 0.03	3.36 ± 0.13	4.63 ± 0.22
2925	304 ± 9	26.5 ± 1.2	23.0 ± 0.9	0.98 ± 0.03	2.14 ± 0.10	5.66 ± 0.21
2926	342 ± 9	27.7 ± 1.2	25.6 ± 0.9	1.11 ± 0.03	2.24 ± 0.09	6.31 ± 0.21
2927	338 ± 9	28.9 ± 1.2	26.0 ± 0.9	1.09 ± 0.03	2.34 ± 0.10	6.41 ± 0.22
(bulk)	360 ± 11	33.4 ± 1.3	26.8 ± 0.9	1.16 ± 0.04	2.71 ± 0.10	6.60 ± 0.22
2930	92 ± 8	84.4 ± 2.3	14.3 ± 0.8	0.30 ± 0.03	6.84 ± 0.18	3.53 ± 0.21

Table A2.4. *Infinite matrix dose rates determined by HRGS and TSBC ([a]based on dose rate conversion factors in Aikten (1983), Sanderson (1987) and Cresswell* et al. *(2018); [b]average of tube and bulk samples, where available).*

SUTL	HRGS, dry[a] / mGy a^{-1}				
no.	Alpha	Beta	Gamma[b]	TSBC, dry / mGy a^{-1}	FGS, wet / mGy a^{-1}
2914	10.8 ± 0.5	1.21 ± 0.04	0.80 ± 0.03	1.44 ± 0.09	0.31 ± 0.03
2915	8.1 ± 0.3	1.04 ± 0.03	0.63 ± 0.02	1.50 ± 0.09	0.25 ± 0.02
2917	13.6 ± 0.4	1.44 ± 0.03	0.91 ± 0.02	1.75 ± 0.10	0.57 ± 0.05
2918	14.4 ± 0.4	1.53 ± 0.03	1.05 ± 0.03	1.80 ± 0.10	0.48 ± 0.03
2919	16.7 ± 0.5	1.58 ± 0.03	1.16 ± 0.03	1.74 ± 0.10	0.51 ± 0.04
2921	10.3 ± 0.3	0.96 ± 0.03	0.65 ± 0.02	1.12 ± 0.08	0.32 ± 0.02
2922	10.8 ± 0.3	0.96 ± 0.03	0.66 ± 0.02	1.27 ± 0.09	0.39 ± 0.03
2923	12.6 ± 0.4	0.99 ± 0.03	0.76 ± 0.03	1.32 ± 0.09	0.37 ± 0.02
2925	10.1 ± 0.3	1.29 ± 0.03	0.77 ± 0.02	1.71 ± 0.10	0.35 ± 0.02
2926	10.9 ± 0.3	1.43 ± 0.03	0.85 ± 0.02	1.82 ± 0.10	0.36 ± 0.03
2927	11.2 ± 0.3	1.43 ± 0.03	0.90 ± 0.03	1.78 ± 0.10	0.30 ± 0.02
2930	21.6 ± 0.5	1.35 ± 0.03	1.04 ± 0.02	1.35 ± 0.09	0.40 ± 0.01

disc and their combined sets. Dose response curves (shown in Supplement B Figures SB.1–SB.12) for each of the preheating temperature groups and the combined data were determined using a fit to a saturating exponential function. There was no evidence of significant differences in normalized OSL ratios (both in natural and regenerated dose points) between subsets of discs pre-heated at temperatures from 200° to 270° C. Accordingly composite dose response curves from selected discs for each sample were constructed and used to estimate equivalent dose values for each individual discs and their combined sets.

Three average values were calculated from the dose estimates from individual aliquots for each

Table A2.5. *Effective beta and gamma dose rates following water correction ([a] Effective beta dose rate combining water content corrections with inverse grain size attenuation factors obtained by weighting the 90–150[b] µm attenuation factors of Mejdahl (1979) for K, U, and Th by the relative beta dose contributions for each source determined by Gamma Spectrometry; [d] includes a cosmic dose contribution).*

	Water contents / %			Effective Dose Rate[a] / mGy a^{-1}		
SUTL no.	Field	Sat	Assumed	Beta[b]	Gamma	Total[b,d]
2914	26	34	30 ± 5	0.89 ± 0.08	0.46 ± 0.05	1.51 ± 0.09
2915	16	38	30 ± 5	0.86 ± 0.07	0.36 ± 0.03	1.39 ± 0.08
2917	6	18	15 ± 5	1.24 ± 0.10	0.68 ± 0.07	2.09 ± 0.12
2918	6	20	15 ± 5	1.29 ± 0.11	0.69 ± 0.06	2.15 ± 0.12
2919	9	23	15 ± 5	1.28 ± 0.11	0.75 ± 0.07	2.20 ± 0.13
2921	3	21	10 ± 5	0.85 ± 0.08	0.45 ± 0.04	1.47 ± 0.09
2922	4	19	10 ± 5	0.91 ± 0.09	0.49 ± 0.05	1.57 ± 0.10
2923	4	27	10 ± 5	0.94 ± 0.09	0.53 ± 0.05	1.64 ± 0.10
2925	15	24	20 ± 5	1.11 ± 0.10	0.49 ± 0.04	1.78 ± 0.10
2926	16	24	20 ± 5	1.21 ± 0.10	0.53 ± 0.05	1.90 ± 0.11
2927	15	34	20 ± 5	1.19 ± 0.10	0.52 ± 0.04	1.88 ± 0.11
2930	14	20	17 ± 3	1.00 ± 0.08	0.64 ± 0.03	1.81 ± 0.09

Table A2.6. *SAR quality parameters.*

SUTL No.	Sensitivity (c Gy^{-1})	Sensitivity change (% per cycle)	Recycling ratio	Zero cycle	IRSL (%)
2914	5900 ± 750	15 ± 3	1.01 ± 0.01	0.04 ± 0.01	0.22 ± 0.18
2915	5240 ± 530	13 ± 2	1.05 ± 0.01	0.04 ± 0.01	0.00 ± 0.03
2917	188 ± 142	4.5 ± 4.1	0.90 ± 0.05†	0.07 ± 0.02†	0.02 ± 0.44
2918	1750 ± 250	5.0 ± 1.1	1.01 ± 0.05	0.09 ± 0.05	0.06 ± 0.21
2919	900 ± 175	9.2 ± 2.2	0.96 ± 0.06	0.06 ± 0.06	0.40 ± 0.57
2921	2540 ± 1050	8.8 ± 4.8	1.02 ± 0.05	0.10 ± 0.07	0.45 ± 0.23
2922	1700 ± 380	9.6 ± 3.1	1.06 ± 0.12	0.08 ± 0.04	0.42 ± 0.35
2923	470 ± 170	15 ± 8	1.25 ± 0.06†	0.00 ± 0.09	0.84 ± 1.70
2925	11600 ± 2500	8.1 ± 2.2	0.99 ± 0.01	0.04 ± 0.01	-0.02 ± 0.04
2926	7980 ± 940	14 ± 2	0.99 ± 0.01	0.03 ± 0.01	-0.02 ± 0.03
2927	12900 ± 1300	12 ± 2	1.02 ± 0.01	0.03 ± 0.01	-0.01 ± 0.06
2930	4420 ± 650	24 ± 4	0.95 ± 0.01	0.03 ± 0.01	0.12 ± 0.07

† Weighted mean used to reduce influence of low precision aliquots

sample, the mean, a weighted mean and the robust mean. These are given in Table 3.7. Probability density functions (pdfs) and abanico plots were generated to describe the dose distributions. The pdfs are shown in Figures A2.21–A2.25, grouping the samples from each site, with the abanico plots in Supplement C Figures SC.1–SC.12.

For the Ġgantija samples (SUTL2914–2915), Figure A2.21, it can be seen that the pdfs for both samples form approximately Gaussian peaks centred on the mean value, with evidence of a tail to higher doses. There is no significant difference between the different averages, and so the mean was taken as the preferred estimate for the stored dose.

Similarly, for the Skorba samples (SUTL2925–2927) (Fig. A2.24), two of the pdfs have approximately Gaussian shapes whereas SUTL2926 is bimodal. The three different averages are, again, very similar and the slightly higher precision weighted mean has been used as the preferred estimate for the stored dose.

For the samples from Marsalforn (SUTL2917–2919) and Ramla (SUTL2921–2923) (Figs. A2.22 & A2.23), the pdfs are generally complex with very broad distributions and multiple peaks. SUTL2918 and 2923 show approximately Gaussian shapes, with tails to high dose rates. In both cases the weighted mean approximates to the position of the peak with better precision, and has been used as the preferred estimate

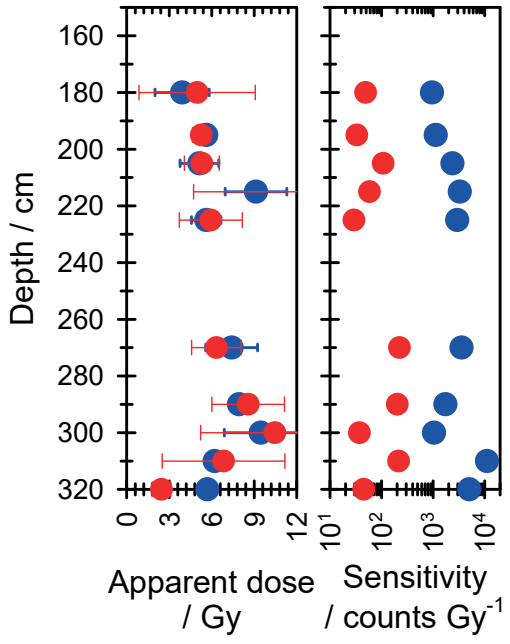

Figure A2.14. *Apparent dose and sensitivity for laboratory OSL (blue) and IRSL (red) profile measurements for SUTL2916 (P1).*

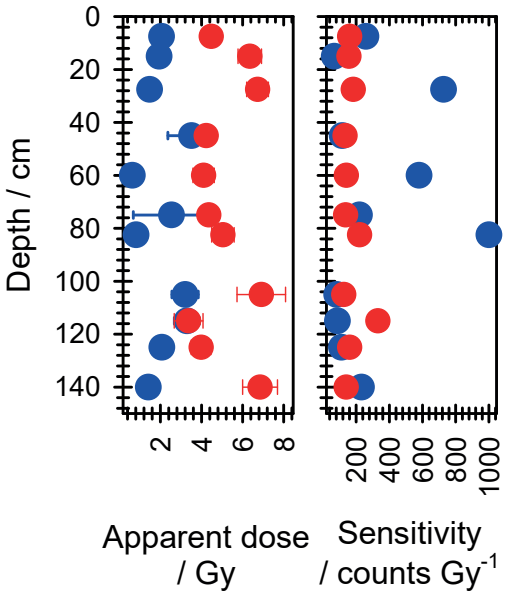

Figure A2.15. *Apparent dose and sensitivity for laboratory OSL (blue) and IRSL (red) profile measurements for SUTL2920 (P2).*

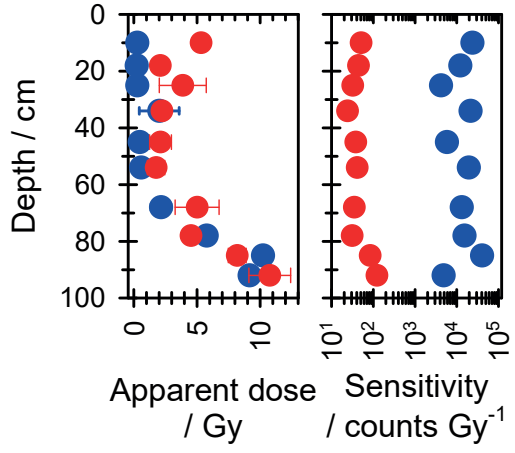

Figure A2.16. *Apparent dose and sensitivity for laboratory OSL (blue) and IRSL (red) profile measurements for SUTL2913 (P3).*

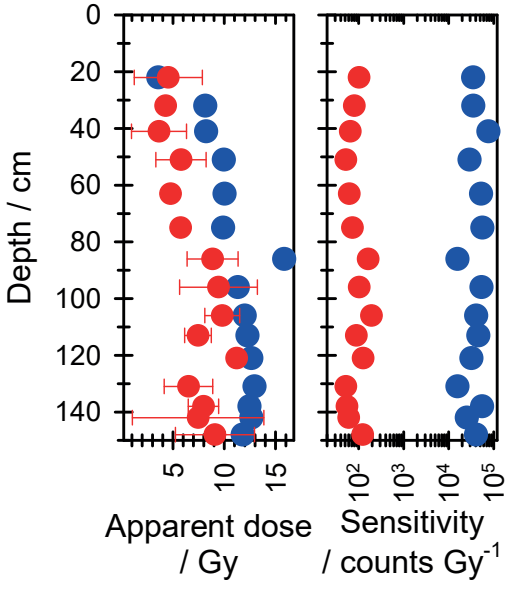

Figure A2.17. *Apparent dose and sensitivity for laboratory OSL (blue) and IRSL (red) profile measurements for SUTL2924 (P4).*

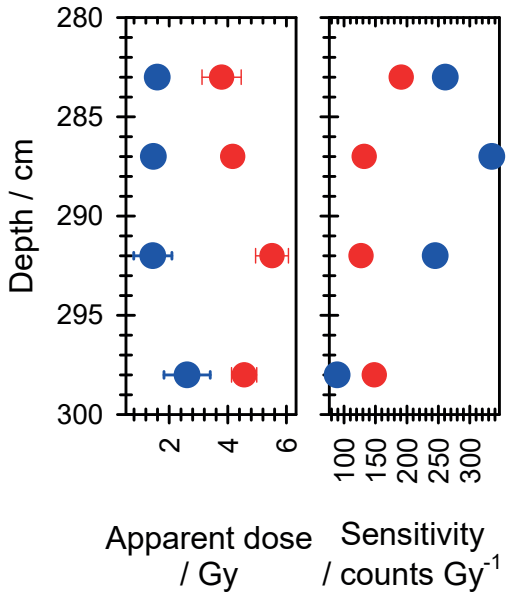

Figure A2.18. *Apparent dose and sensitivity for laboratory OSL (blue) and IRSL (red) profile measurements for SUTL2929 (P5).*

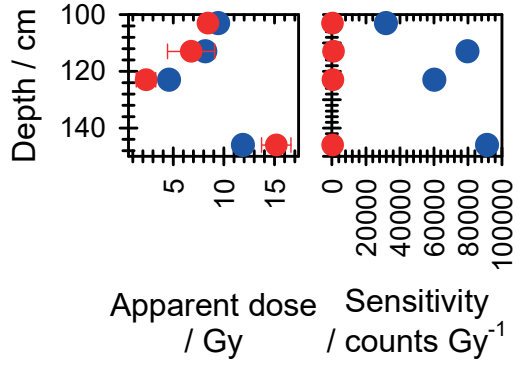

Figure A2.20. *Apparent dose and sensitivity for laboratory OSL (blue) and IRSL (red) profile measurements for SUTL2931 (P7).*

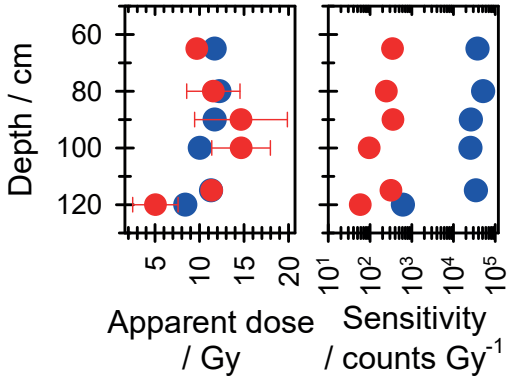

Figure A2.19. *Apparent dose and sensitivity for laboratory OSL (blue) and IRSL (red) profile measurements for SUTL2928 (P6).*

for the stored dose. SUTL2917 shows a very broad peak, with no readily defined preferred stored dose, and the weighted mean has been used since this is generally the preferred value in this project. SUTL2919 shows a lower peak at ~5 Gy which corresponds to a single aliquot, and the mean has been used as the preferred value as this best represents the remaining aliquots. SUTL2921 and 2922 both show multiple peaks, each supported by more than one aliquot. In both cases the weighted mean approximates to the lowest dose peak, and has been preferred.

The sample from Tal-Istabal, Qormi (SUTL2930) (Fig. A2.25), shows a large dominant peak, with two smaller peaks at higher doses. Both the weighted and robust means approximate to the position of this peak, and the slightly higher precision weighted mean has been preferred.

A2.6.3. Age determinations

The total dose rate is determined from the sum of the equivalent beta and gamma dose rates, and the cosmic dose rate. Age estimates are determined by dividing the equivalent stored dose by the dose rate (Table A2.8).

The dose rates for the laboratory profile samples can be estimated by interpolating and extrapolating from the dose rates measured from the OSL samples. This allows an apparent age for the profile samples to be estimated from the apparent doses estimated from the laboratory profile analyses. These are shown in Supplement D Figures SD.1–SD.6.

Table A2.7. *Comments on equivalent dose distributions of SUTL2914 to SUTL2930; preferred estimates in bold (errors stated: ± weighted standard deviation or weighted error).*

SUTL no.	n	Comments on apparent age distribution / individual samples	Mean	Weighted Mean	Robust Mean
2914	8		**4.77 ± 0.25**	4.61 ± 0.13	4.70 ± 0.23
2915	16		**15.0 ± 0.4**	14.7 ± 0.2	15.0 ± 0.4
2917	12	Generally very poor statistics throughout. Dispersed apparent ages	10.8 ± 4.9	**5.8 ± 1.9**	7.3 ± 2.1
2918	16	One significant outlier (67 ± 48 Gy) excluded from means	9.5 ± 1.0	**7.7 ± 0.3**	9.2 ± 0.9
2919	8	One aliquot with Ed = 4.9 ± 0.3 Gy. Remaining aliquots 6.7–10.4 Gy	**7.7 ± 0.6**	6.3 ± 0.2	7.8 ± 0.6
2921	8	Large dispersion of Ed values	1.3 ± 0.7	**0.20 ± 0.02**	0.83 ± 0.34
2922	8		0.48 ± 0.09	**0.26 ± 0.01**	0.52 ± 0.11
2923	8	Large dispersion of Ed values	0.12 ± 0.50	**0.17 ± 0.05**	0.39 ± 0.32
2925	16		17.6 ± 0.4	**17.4 ± 0.2**	17.5 ± 0.5
2926	16	12 aliquots with Ed 17.0–19.6 Gy. 4 aliquots with Ed 21.0–23.0 Gy.	19.6 ± 0.5	**19.2 ± 0.2**	19.6 ± 0.6
2927	16		20.8 ± 0.6	**20.3 ± 0.6**	20.5 ± 0.5
2930	12		0.81 ± 0.08	**0.72 ± 0.02**	0.74 ± 0.04

Table A2.8. *Quartz OSL sediment ages.*

SUTL no.	Dose (Gy)	Dose Rate (mGy a^{-1})	Years / ka	Calendar years
2914	4.77 ± 0.25	1.51 ± 0.09	3.16 ± 0.25	1140±250 BC
2915	15.0 ± 0.4	1.39 ± 0.08	10.79 ± 0.68	8770±680 BC
2917	5.8 ± 1.9	2.09 ± 0.12	2.78 ± 0.92	760±920 BC
2918	7.7 ± 0.3	2.15 ± 0.12	3.58 ± 0.24	1560±240 BC
2919	7.7 ± 0.6	2.20 ± 0.13	3.50 ± 0.34	1480±340 BC
2921	0.20 ± 0.02	1.47 ± 0.09	0.14 ± 0.02	AD 1880±16
2922	0.26 ± 0.01	1.57 ± 0.10	0.17 ± 0.01	AD 1850±12
2923	0.17 ± 0.05	1.64 ± 0.10	0.10 ± 0.03	AD 1910±30
2925	17.4 ± 0.2	1.78 ± 0.10	9.78 ± 0.56	7760±560 BC
2926	19.2 ± 0.2	1.90 ± 0.11	10.11 ± 0.59	8090±590 BC
2927	20.3 ± 0.6	1.88 ± 0.11	10.80 ± 0.71	8780±710 BC
2930	0.72 ± 0.02	1.81 ± 0.09	0.40 ± 0.02	AD 1620±23

A2.7. Discussion

The dates determined from the OSL measurements and their contexts are summarized in Tables A2.8 and A2.9.

A2.7.1. Ġgantija Temple (SUTL2914 and 2915)

The samples were taken from a reopened test pit, initially excavated in 2014, on the western edge of the platform south of Ġgantija temple, which showed agricultural soil build-up over an *in situ* buried soil. Profiling shows low apparent dose (approximately 1 Gy or less, in most cases corresponding to an apparent age of a few centuries) for the agricultural soil, with a significant increase in dose with depth for the buried soil. The samples for OSL dating were taken from immediately below the base of the agricultural soil and the base of the buried soil. For SUTL2914 immediately below the agricultural soil the estimated stored doses and corresponding ages are consistent, and confirms that the agricultural soil is modern, and that the buries soil is prehistoric (older than 1000 BC). The date determined for the onset of the soil accumulation from SUTL2915 (8770±680 BC) is older than the apparent age from the corresponding profile sample (~5000 BC) and both age estimates significantly pre-date Neolithic human activity on the islands, and the initial construction of the Ġgantija temples (3600 BC). The date for the final exposure of the soil (1140±250 BC) is in the Bronze Age,

Table A2.9. *Locations, dates and archaeological significance of sediment samples SUTL2914–2930 (Dates in italics are poorly constrained due to low precision and large dispersion of equivalent doses determined by OSL analysis).*

Sample ID	SUTL no.	Depth /cm	Date	Archaeological significance
Marsalforn valley				
OSL1	2917	175–180	*760±920 BC*	Constrains the final period that the upper incipient soil in hillwash was exposed, phase 2
OSL2	2918	265–270	1560±240 BC	Constrains the final period that the lower incipient soil in hillwash was exposed, phase 1
OSL3	2919	320–330	1480±340 BC	Constrains the onset of hillwash accumulation, phase 1
Ramla valley				
OSL4	2921	15–20	*AD 1880±16*	Provides a temporal constraint on degradation of upper slope
OSL5	2922	62–66	AD 1850±12	Provide temporal constraints on periods of colluviation
OSL6	2923	103–106	*AD 1910±30*	
Ġgantija Temple				
OSL7	2914	78	1140±250 BC	Constrains the final period that the buried soil was exposed
OSL8	2915	92	8770±680 BC	Constrains onset of soil formation
Tal-Istabal, Qormi				
OSL9	2930	295–298	AD 1620±23	Constrains the burial of soil
Skorba Neolithic site				
OSL10	2925	118	7760±560 BC	Constrains the final period that the buried soil was exposed
OSL11	2926	128	8090±590 BC	Constrains the age of the buried land surface
OSL12	2927	145	8780±710 BC	Constrains onset of soil formation

significantly later than the last stages of construction at the temples (2500 BC). However, there is evidence of Bronze Age activity at other Neolithic sites in the islands.

A2.7.2. Ramla and Marsalforn Valleys (SUTL2917–2923)

The Ramla valley, and the tributary Marsalforn valley, form the southern boundary of the Xagħra plateau, on which the Neolithic temple site of Ġgantija is located. It is known that the plateau is largely denuded of Holocene soils, which are concentrated in the valleys. The OSL investigations in these valleys were undertaken with the aim of generating a chronology for the sequences of buried palaeosols, hillwash and alluvial deposits preserved there. The OSL dates for these materials are generally poorly constrained due to poor signal and dispersed stored doses, suggesting considerable re-working of material.

For Marsalforn Valley, the upper-most sample (SUTL2917) could not be dated, with the ages for the lower two samples consistent with being the same age (SUTL2918 1560±240 BC, SUTL2919 1480±340 BC). These are also consistent with the apparent ages from the profile measurements, which suggest a gradual increase in age from approximately 2–3.5 ka over the 180 to 290 cm depth range, with a slight inversion to younger ages below that. The impressions from the field and laboratory profiles that this section represents gradual accumulation of material is not contradicted by the OSL dates for the upper samples given the poor precision of SUTL2917 and the general agreement between OSL ages and profile apparent ages for the lower samples, giving an accumulation rate for the upper part of the section of approximately 1 m ka^{-1}. However, the data suggest that the lower part of the section (290–320 cm depth) accumulated rapidly, with the inverted apparent age profile suggesting better zeroed material being deposited first.

The Ramla Valley dating samples (SUTL2921–2923) are all modern, with OSL dates in the nineteenth and early twentieth centuries AD, based on the youngest component in the dose distributions, although it is noted that these distributions also contain older components and that the apparent ages from the profile samples are significantly older (0.5–2.0 ka, with the best constrained apparent ages at 0.5–1.0 ka). This supports the inference from the field and laboratory profiling that this material was deposited over a short period of time.

A2.7.3. Skorba Neolithic site (SUTL2925–2927)

Excavations on the western edge of the Skorba temple/settlement revealed three curvilinear stone walls of the Neolithic period effectively sealing an accumulated soil. The profile samples indicate a gradual increase in

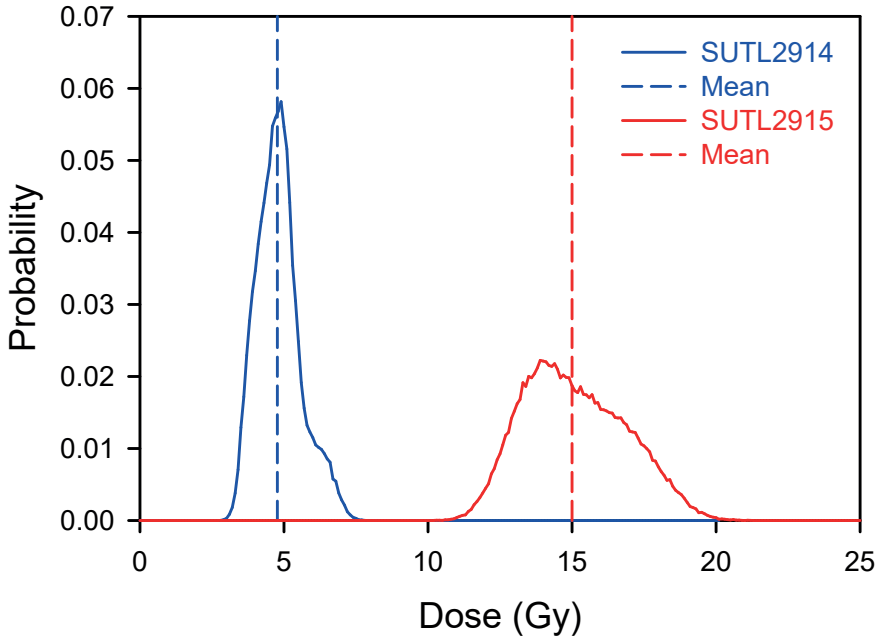

Figure A2.21. *Probability Distribution Functions for the stored dose on samples SUTL2914 and 2915.*

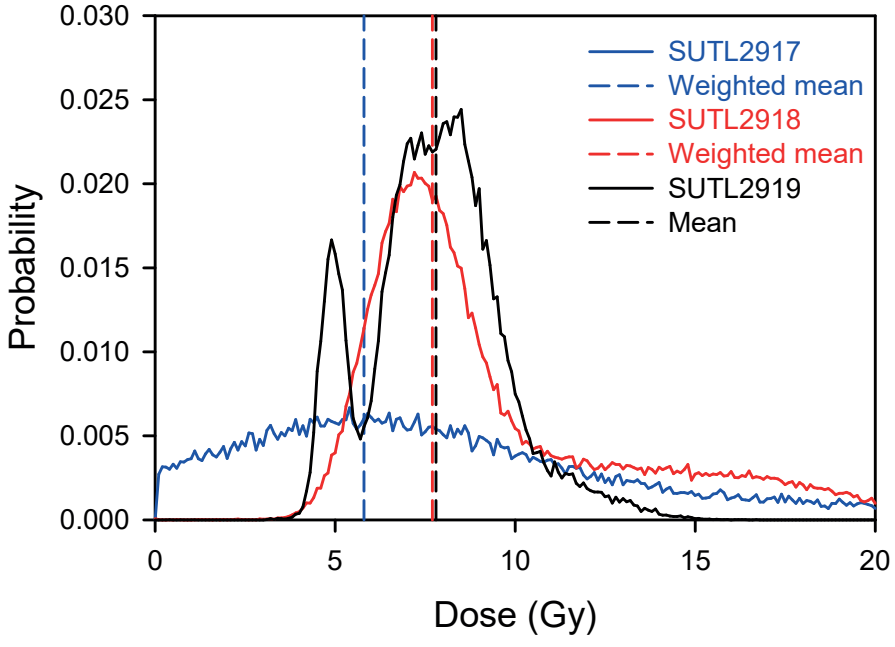

Figure A2.22. *Probability Distribution Functions for the stored dose on samples SUTL2917–2919. Note, SUTL2918 includes a single aliquot with a stored dose of 67 ± 48 Gy.*

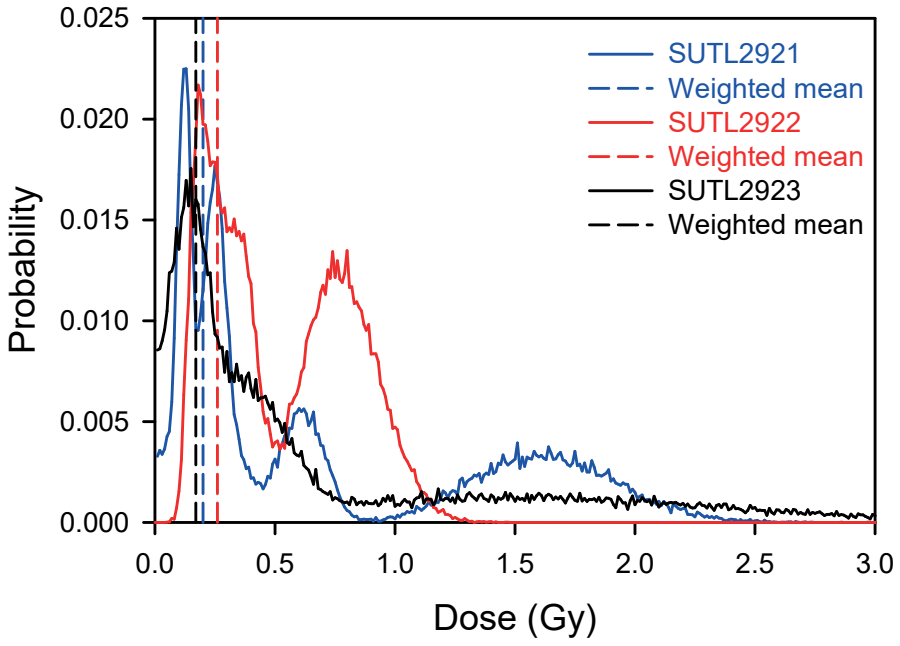

Figure A2.23. *Probability Distribution Functions for the stored dose on samples SUTL2921–2923. Note, SUTL2921 includes a single aliquot with a stored dose of 5.8 ± 0.9 Gy.*

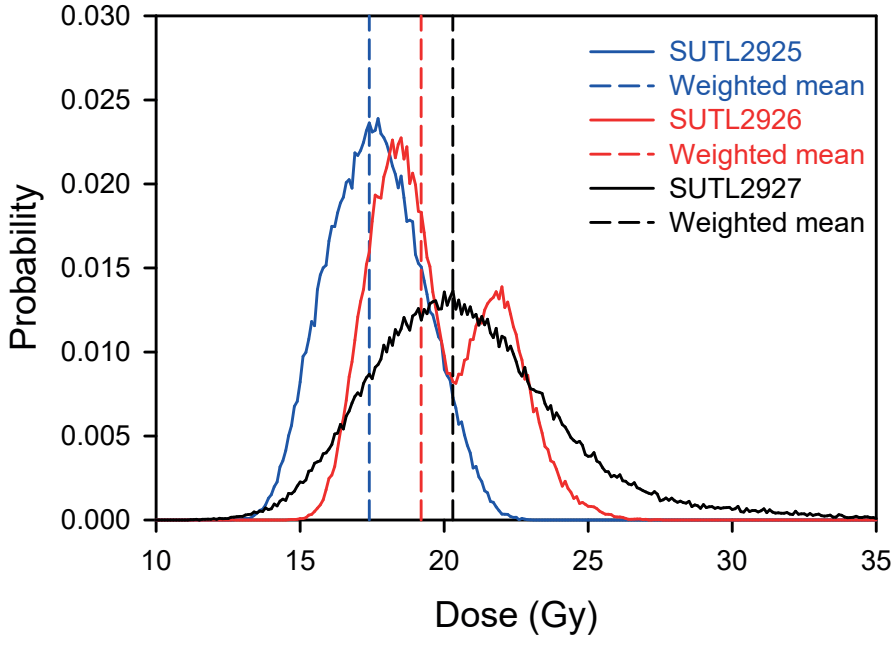

Figure A2.24. *Probability Distribution Functions for the stored dose on samples SUTL2925–2927.*

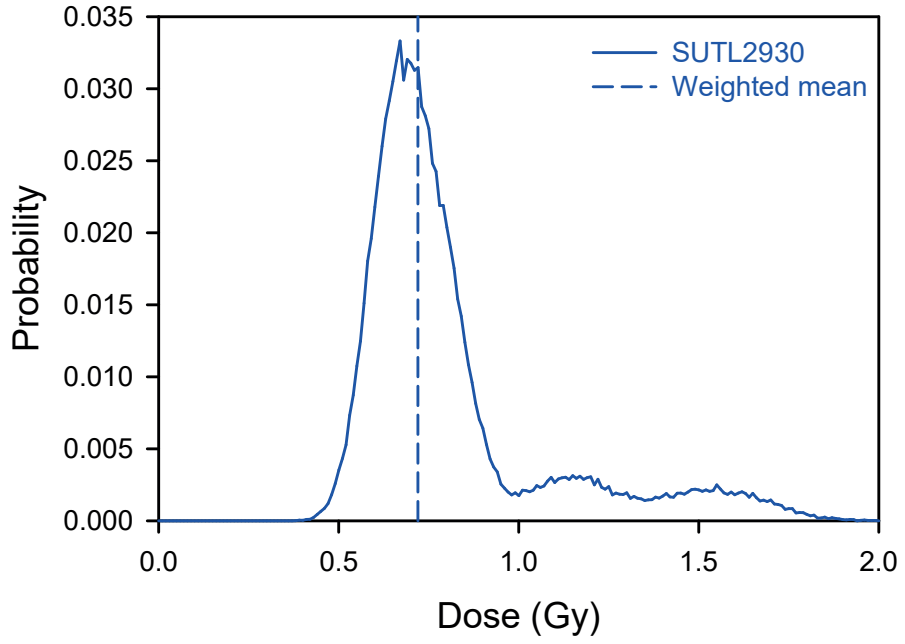

Figure A2.25. *Probability Distribution Function for the stored dose on sample SUTL2930.*

stored dose with depth, with no clear change in stored dose below the Neolithic structure. The profile apparent age estimates show generally very good agreement between equivalent contexts in profiles 4 and 6, with a couple of exceptions. The uppermost profile sample shows an apparent age of approximately 2.0 ka, with the remaining samples showing a gradual increase in apparent age from approximately 5.0 to 7.0 ka down the sections. These are lower than the ages obtained for the OSL dating samples, with a very similar pattern to the bottom sample of profile 3 at the Ġgantija site. The OSL dating samples were selected to constrain the period of accumulation of this soil. The onset of soil accumulation (8780±710 BC) is consistent with the onset of soil accumulation at the Ġgantija site (SUTL2915 8770±680 BC). The upper two samples produce consistent OSL dates (7760±560 BC and 8090±590 BC) which are significantly older than the earliest known human activity in the vicinity (5000 BC) (Trump 1966). These samples are located below the context that had been suggested corresponded to the context at the base of the Trump (1966) excavation.

A2.7.4. Tal-Istabal, Qormi (SUTL2930)

Within excavations of a large Punic-Roman area of terraces and irrigation features *c*. 30–40 cm of agricultural/buried soil was sampled beneath a surviving wall. The laboratory and field profile measurements indicated a slight increase in stored dose with depth below the wall, which is reflected in the apparent age estimates, which carry large uncertainties. The OSL date (AD 1620±23) significantly post-dates the Roman period, lower than the apparent ages from the profiling for the upper three samples (AD 1200±250), which would still result in a post-Roman date. These young ages for material from beneath a surviving Punic-Roman age wall are unexpected.

A2.8. Conclusions

Despite the local limestone geology not supplying abundant quantities of silicates to the soils and sediments at these sites, micromorphological studies had already shown the presence of small quantities of silicate minerals. Both field and laboratory profiling measurements had indicated that these minerals carry measurable luminescence signals, with the OSL signals associated with quartz the most promising for dating. Although the quartz yields from the samples collected for OSL dating were limited the signals from the quartz grains extracted were generally bright, in most cases providing sufficient signal to quantify the

ages of the sampled sediments and soils. It is known that dust from the Sahara has been transported across the Mediterranean, and beyond, for approximately five million years and that this has contributed to the soils on Malta and Gozo. The large signals observed from the quartz grains studied here are similar to those observed from Saharan sand, supporting that source for the silicates measured. This work has demonstrated that even in locations where the local geology is deficient in quartz OSL measurements can be conducted using aeolian quartz from more distant sources. In locations where this primary aeolian mineral input is preserved this should retain a palaeoclimatic signal combining aridity history in the Saharan source regions and wind patterns that move these minerals across the Mediterranean region.

For most of the samples collected from hillwash and alluvial deposits in valleys the equivalent doses showed variations of a factor of two to three between aliquots, reflecting inhomogeneous or partial bleaching of the quartz grains in these samples. This suggests that the erosion and sediment transport processes resulting in these deposits did not expose the minerals to sufficient light to remove all the residual signals from burial in earlier sediments. This could be the result of bulk movement of sediment or the rapid erosion, movement and re-burial of the minerals. Although reliable dates were not always quantifiable, the data do provide information about the processes of formation for these deposits.

For the soils directly associated with the temple sites the equivalent dose values did not show significant dispersion, suggesting that the quartz grains had been well zeroed prior to burial and that there has not been substantial disturbance since then. This allowed ages to be determined even from the small number of aliquots available. This has demonstrated that OSL dating provides valuable information, and should be applied in any further studies of these and similar monuments.

Appendix 2 – Supplement A

Table SA.1. *Field profiling data, as obtained using portable OSL equipment, for the sediment stratigraphies examined on Gozo and Malta.*

Sample no.	IRSL net signal intensities	IRSL depletion ratio	OSL net signal intensities	OSL depletion ratio	IRSL/OSL ratio
P1/1	2178 ± 66	1.26 ± 0.06	35102 ± 194	2.37 ± 0.03	0.0620 ± 0.0019
P1/2	14293 ± 129	1.51 ± 0.03	103206 ± 325	2.12 ± 0.01	0.1385 ± 0.0013
P1/3	4997 ± 86	1.39 ± 0.04	59909 ± 250	1.98 ± 0.02	0.0834 ± 0.0015
P1/4	5290 ± 86	1.54 ± 0.05	73218 ± 275	2.02 ± 0.02	0.0722 ± 0.0012
P1/5	5817 ± 89	1.40 ± 0.04	66796 ± 263	1.91 ± 0.02	0.0871 ± 0.0014
P1/6	4077 ± 80	1.25 ± 0.04	54936 ± 240	2.34 ± 0.02	0.0742 ± 0.0015
P1/7	3935 ± 80	1.34 ± 0.05	46536 ± 222	2.06 ± 0.02	0.0846 ± 0.0018
P1/8	2804 ± 74	1.40 ± 0.06	53609 ± 238	2.43 ± 0.02	0.0523 ± 0.0014
P1/9	3692 ± 77	1.43 ± 0.05	50362 ± 230	2.48 ± 0.02	0.0733 ± 0.0016
P1/10	19162 ± 148	1.73 ± 0.03	81874 ± 291	2.54 ± 0.02	0.2340 ± 0.0020
P2/1	4792 ± 81	1.46 ± 0.05	90499 ± 304	2.79 ± 0.02	0.0530 ± 0.0009
P2/2	2261 ± 66	1.30 ± 0.06	38257 ± 201	2.09 ± 0.02	0.0591 ± 0.0017
P2/3	3511 ± 76	1.54 ± 0.06	21854 ± 155	1.73 ± 0.02	0.1607 ± 0.0036
P2/4	454 ± 49	1.16 ± 0.12	11777 ± 118	1.56 ± 0.03	0.0385 ± 0.0042
P2/5	818 ± 54	1.55 ± 0.12	13389 ± 124	1.66 ± 0.03	0.0611 ± 0.0041
P2/6	1161 ± 55	1.46 ± 0.10	17459 ± 140	2.07 ± 0.03	0.0665 ± 0.0032
P2/7	980 ± 54	1.44 ± 0.11	16591 ± 137	1.43 ± 0.02	0.0591 ± 0.0033
P2/8	1151 ± 55	1.14 ± 0.08	18251 ± 142	1.93 ± 0.03	0.0631 ± 0.0030
P2/9	836 ± 51	1.21 ± 0.10	7448 ± 96	1.64 ± 0.04	0.1122 ± 0.0070
P2/10	659 ± 49	1.16 ± 0.11	11238 ± 115	1.41 ± 0.03	0.0586 ± 0.0044
P2/11	11480 ± 115	1.57 ± 0.03	49486 ± 228	2.09 ± 0.02	0.2320 ± 0.0026
P3/1	359 ± 45	1.76 ± 0.21	12511 ± 119	2.99 ± 0.06	0.0287 ± 0.0036
P3/2	-	-	6605 ± 93	3.28 ± 0.10	
P3/3	-	-	5468 ± 90	3.48 ± 0.12	
P3/4	-	-	7899 ± 98	2.49 ± 0.07	
P3/5	275 ± 42	1.43 ± 0.20	10350 ± 110	3.94 ± 0.10	0.0266 ± 0.0040
P3/6	207 ± 43	1.03 ± 0.14	12783 ± 120	3.07 ± 0.07	0.0162 ± 0.0034
P3/7	245 ± 44	2.89 ± 0.40	12328 ± 119	2.42 ± 0.05	0.0199 ± 0.0036
P3/8	-	-	22897 ± 164	2.50 ± 0.04	
P3/9	1912 ± 62	1.66 ± 0.09	74749 ± 277	2.41 ± 0.02	0.0256 ± 0.0008
P3/10	1967 ± 62	1.44 ± 0.07	80253 ± 287	2.47 ± 0.02	0.0245 ± 0.0008

Table SA.1 *(cont.).*

Sample no.	IRSL net signal intensities	IRSL depletion ratio	OSL net signal intensities	OSL depletion ratio	IRSL/OSL ratio
P4/15	5995 ± 88	1.63 ± 0.05	240349 ± 493	2.46 ± 0.01	0.0249 ± 0.0004
P4/14	5177 ± 87	1.51 ± 0.05	226018 ± 478	2.54 ± 0.01	0.0229 ± 0.0004
P4/13	5712 ± 90	1.41 ± 0.04	211440 ± 462	3.09 ± 0.02	0.0270 ± 0.0004
P4/12	5291 ± 87	1.37 ± 0.04	225233 ± 477	2.50 ± 0.01	0.0235 ± 0.0004
P4/11	5240 ± 88	1.50 ± 0.04	213038 ± 465	2.48 ± 0.01	0.0246 ± 0.0004
P4/10	4344 ± 82	1.42 ± 0.05	184363 ± 432	2.48 ± 0.01	0.0236 ± 0.0004
P4/9	3525 ± 77	1.49 ± 0.06	168705 ± 414	2.43 ± 0.01	0.0209 ± 0.0005
P4/8	2397 ± 73	1.53 ± 0.07	123329 ± 355	2.49 ± 0.02	0.0194 ± 0.0006
P4/7	2331 ± 73	1.52 ± 0.07	114334 ± 342	2.69 ± 0.02	0.0204 ± 0.0006
P4/6	2312 ± 70	1.41 ± 0.06	119908 ± 350	2.56 ± 0.02	0.0193 ± 0.0006
P4/5	1670 ± 70	1.67 ± 0.08	111527 ± 339	2.45 ± 0.02	0.0150 ± 0.0006
P4/4	2896 ± 80	1.47 ± 0.06	138249 ± 376	2.84 ± 0.02	0.0209 ± 0.0006
P4/3	1227 ± 64	1.43 ± 0.08	130444 ± 365	2.61 ± 0.02	0.0094 ± 0.0005
P4/2	1443 ± 65	1.41 ± 0.08	72598 ± 274	2.53 ± 0.02	0.0199 ± 0.0009
P4/1	796 ± 60	1.71 ± 0.12	51567 ± 233	2.84 ± 0.03	0.0154 ± 0.0012
P5/1	422 ± 62	1.20 ± 0.12	12643 ± 125	3.23 ± 0.07	0.0334 ± 0.0049
P5/2	535 ± 60	1.55 ± 0.15	9533 ± 113	3.04 ± 0.08	0.0561 ± 0.0064
P5/3	730 ± 62	1.99 ± 0.18	14463 ± 134	2.69 ± 0.05	0.0505 ± 0.0043
P5/4	502 ± 62	1.64 ± 0.15	15182 ± 135		0.0331 ± 0.0041
P6/1	-	-	133503 ± 377	2.34 ± 0.01	
P6/2	3808 ± 71	1.36 ± 0.05	139097 ± 375	2.25 ± 0.01	0.0274 ± 0.0005
P6/3	-	-	125277 ± 365	2.38 ± 0.01	
P6/4	3547 ± 71	1.29 ± 0.05	125270 ± 357	2.38 ± 0.01	0.0283 ± 0.0006
P6/5	2451 ± 64	1.41 ± 0.06	99668 ± 319	2.19 ± 0.02	0.0246 ± 0.0006
P6/6	4579 ± 79	1.41 ± 0.04	186586 ± 434	2.39 ± 0.01	0.0245 ± 0.0004

Table SA.2. *OSL screening measurements on paired aliquots of 90–250 μm 40% HF-etched 'quartz'.*

SUTL no.	Field ID	Stored dose / Gy		Sensitivity / photon counts Gy^{-1}		/ Gy	/ photon counts Gy^{-1}
		Aliquot 1	Aliquot 2	Aliquot 1	Aliquot 2	Mean	
2916A	P1/1	5.82 ± 0.24	2.00 ± 0.18	1506 ± 39	389 ± 20	3.91 ± 1.91	948 ± 559
2916B	P1/2	5.62 ± 0.25	28.35 ± 1.39	1222 ± 35	1017 ± 32	16.98 ± 11.37	1120 ± 103
2916C	P1/3	3.76 ± 0.47	6.49 ± 0.15	201 ± 14	4550 ± 67	5.13 ± 1.37	2376 ± 2174
2916D	P1/4	6.95 ± 0.25	11.30 ± 0.24	1516 ± 39	5046 ± 71	9.12 ± 2.17	3281 ± 1764
2916E	P1/5	4.57 ± 0.48	6.65 ± 0.13	220 ± 15	5627 ± 75	5.61 ± 1.04	2924 ± 2703
2916F	P1/6	5.58 ± 0.17	9.23 ± 0.21	2764 ± 53	4319 ± 66	7.40 ± 1.83	3541 ± 777
2916G	P1/7	7.83 ± 0.31	8.02 ± 0.26	1354 ± 37	2099 ± 46	7.92 ± 0.24	1726 ± 373
2916H	P1/8	12.02 ± 0.71	6.89 ± 0.31	843 ± 29	1240 ± 35	9.45 ± 2.57	1041 ± 199
2916I	P1/9	5.93 ± 0.11	6.48 ± 0.08	7038 ± 84	15101 ± 123	6.20 ± 0.27	11070 ± 4031
2916J	P1/10	6.35 ± 0.21	5.03 ± 0.09	2390 ± 49	7691 ± 88	5.69 ± 0.66	5040 ± 2650
2920A	P2/1	2.05 ± 0.24		259 ± 16		2.05 ± 0.24	259 ± 16
2920B	P2/2	1.93 ± 0.47		68 ± 8		1.93 ± 0.47	68 ± 8
2920C	P2/3	1.47 ± 0.10		727 ± 27		1.47 ± 0.10	727 ± 27
2920D	P2/4	4.66 ± 1.00	2.35 ± 0.45	85 ± 9	148 ± 12	3.51 ± 1.63	116 ± 45
2920E	P2/5	0.63 ± 0.07		579 ± 24		0.63 ± 0.07	579 ± 24

Table SA.2 *(cont.).*

SUTL no.	Field ID	Stored dose / Gy		Sensitivity / photon counts Gy^{-1}		/ Gy	/ photon counts Gy^{-1}
		Aliquot 1	Aliquot 2	Aliquot 1	Aliquot 2	Mean	
2920F	P2/6	0.68 ± 0.09	4.40 ± 1.11	381 ± 20	59 ± 8	2.54 ± 2.63	220 ± 228
2920G	P2/7	0.81 ± 0.06		1000 ± 32		0.81 ± 0.06	1000 ± 32
2920H	P2/8	3.20 ± 0.64		83 ± 9		3.20 ± 0.64	83 ± 9
2920I	P2/9	3.29 ± 0.61		87 ± 9		3.29 ± 0.61	87 ± 9
2920J	P2/10	2.07 ± 0.40		111 ± 11		2.07 ± 0.40	111 ± 11
2920K	P2/11	1.41 ± 0.22		232 ± 15		1.41 ± 0.22	232 ± 15
2913A	P3/1	0.33 ± 0.01	0.200 ± 0.003	6948 ± 83	40747 ± 202	0.27 ± 0.07	23848 ± 16900
2913B	P3/2	0.167 ± 0.004	0.27 ± 0.01	20089 ± 142	4222 ± 65	0.22 ± 0.05	12156 ± 7933
2913C	P3/3	0.25 ± 0.01	0.28 ± 0.01	4437 ± 67	3944 ± 63	0.27 ± 0.02	4190 ± 247
2913D	P3/4	0.43 ± 0.01	3.59 ± 0.04	24997 ± 158	17770 ± 133	2.01 ± 1.58	21384 ± 3614
2913E	P3/5	0.56 ± 0.02	0.35 ± 0.01	4973 ± 71	6688 ± 82	0.46 ± 0.10	5831 ± 857
2913F	P3/6	0.48 ± 0.01	0.67 ± 0.01	30097 ± 173	8899 ± 94	0.58 ± 0.09	19498 ± 10599
2913G	P3/7	2.94 ± 0.09	1.36 ± 0.02	2885 ± 54	23541 ± 153	2.15 ± 0.79	13213 ± 10328
2913H	P3/8	5.38 ± 0.06	6.13 ± 0.08	17333 ± 132	13410 ± 116	5.76 ± 0.38	15372 ± 1961
2913I	P3/9	10.12 ± 0.08	10.31 ± 0.07	37034 ± 192	43696 ± 209	10.22 ± 0.09	40365 ± 3331
2913J	P3/10	8.53 ± 0.17	9.79 ± 0.24	5952 ± 77	3745 ± 61	9.16 ± 0.63	4849 ± 1103
2929A	P5/1	1.70 ± 0.26	1.48 ± 0.18	236 ± 15	285 ± 17	1.59 ± 0.16	261 ± 35
2929B	P5/2	1.73 ± 0.27	1.19 ± 0.11	181 ± 13	489 ± 22	1.46 ± 0.38	335 ± 218
2929C	P5/3	0.80 ± 0.10	2.09 ± 0.38	369 ± 19	121 ± 11	1.44 ± 0.92	245 ± 176
2929D	P5/4	3.40 ± 0.72	1.82 ± 0.32	70 ± 8	108 ± 10	2.61 ± 1.12	89 ± 27
2928A	P6/1	11.39 ± 0.08	12.01 ± 0.10	41658 ± 204	33686 ± 184	11.70 ± 0.31	37672 ± 3986
2928B	P6/2	11.92 ± 0.11	12.55 ± 0.11	25557 ± 160	77647 ± 279	12.23 ± 0.31	51602 ± 26045
2928C	P6/3	11.52 ± 0.09	11.86 ± 0.15	38308 ± 196	13986 ± 118	11.69 ± 0.17	26147 ± 12161
2928D	P6/4	9.82 ± 0.09	10.24 ± 0.09	23824 ± 154	27373 ± 165	10.03 ± 0.21	25598 ± 1774
2928E	P6/5	11.78 ± 0.08	10.81 ± 0.10	42131 ± 205	26739 ± 164	11.30 ± 0.48	34435 ± 7969
2928F	P6/6	8.38 ± 0.58	8.43 ± 0.58	615 ± 25	612 ± 25	8.40 ± 0.48	613 ± 21
2931A	P7/1	9.14 ± 0.07	9.70 ± 0.10	42722 ± 207	20750 ± 144	9.42 ± 0.28	31736 ± 10986
2931B	P7/2	8.38 ± 0.04	7.93 ± 0.04	83074 ± 288	76168 ± 276	8.16 ± 0.23	79621 ± 3453
2931C	P7/3	4.93 ± 0.04	4.22 ± 0.02	34230 ± 185	86158 ± 294	4.58 ± 0.35	60194 ± 25964
2931D	P7/4	11.84 ± 0.06	11.89 ± 0.05	80656 ± 284	101688 ± 319	11.87 ± 0.05	91172 ± 10516

Table SA.3. *OSL screening measurements on three aliquots of 90–250 μm 40% HF-etched 'quartz' for SUTL2924.*

SUTL no.	Field ID	Stored dose / Gy			Sensitivity / photon counts Gy^{-1}			/ Gy	/ photon counts Gy^{-1}
		Aliquot 1	Aliquot 2	Aliquot 3	Aliquot 1	Aliquot 2	Aliquot 3	Mean	
2924A	P4/1	3.55 ± 0.03	3.59 ± 0.03	3.56 ± 0.03	27174 ± 165	40827 ± 202	36701 ± 192	3.57 ± 0.02	34901 ± 6827
2924B	P4/2	8.13 ± 0.08	8.38 ± 0.06	7.90 ± 0.06	23619 ± 154	46797 ± 216	35381 ± 188	8.14 ± 0.24	35266 ± 11589
2924C	P4/3	8.49 ± 0.04	7.81 ± 0.05	8.38 ± 0.05	111907 ± 335	57758 ± 240	58463 ± 242	8.23 ± 0.34	76042 ± 27074
2924D	P4/4	10.27 ± 0.09	10.23 ± 0.08	9.36 ± 0.09	25766 ± 161	39058 ± 198	22088 ± 149	9.96 ± 0.45	28971 ± 8485
2924E	P4/5	10.09 ± 0.08	9.74 ± 0.06	10.24 ± 0.06	30295 ± 174	55414 ± 235	70989 ± 266	10.02 ± 0.25	52233 ± 20347
2924F	P4/6	10.00 ± 0.06	9.26 ± 0.06	10.41 ± 0.06	58387 ± 242	47008 ± 217	62521 ± 250	9.89 ± 0.57	55972 ± 7756
2924G	P4/7	15.84 ± 0.19	5.04 ± 0.81	4.64 ± 0.74	15685 ± 125			8.51 ± 5.60	15685 ± 125
2924H	P4/8	11.14 ± 0.07	10.93 ± 0.07	11.91 ± 0.08	55414 ± 235	54789 ± 234	49922 ± 223	11.32 ± 0.49	53375 ± 2746
2924I	P4/9	12.42 ± 0.09	10.99 ± 0.11	12.56 ± 0.08	40395 ± 201	23165 ± 152	58415 ± 242	11.99 ± 0.79	40658 ± 17625
2924J	P4/10	11.78 ± 0.09	12.48 ± 0.09	12.50 ± 0.08	39231 ± 198	43100 ± 208	54282 ± 233	12.26 ± 0.36	45538 ± 7526
2924K	P4/11	12.24 ± 0.10	12.67 ± 0.08	12.99 ± 0.17	29496 ± 172	54219 ± 233	12411 ± 111	12.63 ± 0.38	32042 ± 20904
2924L	P4/12	12.72 ± 0.11	13.16 ± 0.31	4.72 ± 0.80	27041 ± 164	4188 ± 65		10.20 ± 4.22	15615 ± 11426
2924M	P4/13	13.28 ± 0.09	11.89 ± 0.06	12.19 ± 0.10	49639 ± 223	81273 ± 285	34906 ± 187	12.46 ± 0.69	55273 ± 23183
2924N	P4/14	13.05 ± 0.09	12.44 ± 0.17	12.41 ± 0.12	40900 ± 202	11550 ± 107	23300 ± 153	12.63 ± 0.32	25250 ± 14675
2924O	P4/15	12.02 ± 0.25	12.15 ± 0.06	11.25 ± 0.09	5366 ± 73	86947 ± 295	29330 ± 171	11.80 ± 0.45	40548 ± 40790

Table SA.4. *IRSL screening measurements on paired aliquots of 90–250 μm 15% HF-etched 'polymineral' for SUTL2924.*

SUTL no.	Field ID	Stored dose / Gy		Sensitivity / photon counts Gy^{-1}		/ Gy	/ photon counts Gy^{-1}
		Aliquot 1	Aliquot 2	Aliquot 1	Aliquot 2	Mean	
2916A	P1/1	0.87 ± 0.20	9.07 ± 2.99	72 ± 8	26 ± 5	4.97 ± 4.10	49 ± 23
2916B	P1/2	5.87 ± 1.77	4.64 ± 1.29	34 ± 6	32 ± 6	5.26 ± 0.62	33 ± 6
2916C	P1/3	6.53 ± 1.42	4.07 ± 0.63	67 ± 8	147 ± 12	5.30 ± 1.23	107 ± 40
2916D	P1/4	4.72 ± 0.80	99.38 ± 28.49	94 ± 10	23 ± 5	52.05 ± 47.33	58 ± 36
2916E	P1/5	8.15 ± 2.25	3.71 ± 1.12	31 ± 6	27 ± 5	5.93 ± 2.22	29 ± 4
2916F	P1/6	4.58 ± 1.65	8.08 ± 0.76	27 ± 5	416 ± 20	6.33 ± 1.75	222 ± 194
2916G	P1/7	11.14 ± 3.64	6.01 ± 0.56	25 ± 5	376 ± 19	8.57 ± 2.56	201 ± 176
2916H	P1/8	15.68 ± 3.60	5.21 ± 1.50	47 ± 7	27 ± 5	10.45 ± 5.23	37 ± 10
2916I	P1/9	11.16 ± 1.20	2.51 ± 0.50	348 ± 19	80 ± 9	6.83 ± 4.33	214 ± 134
2916J	P1/10	3.12 ± 1.06	1.79 ± 0.54	45 ± 7	44 ± 7	2.45 ± 0.66	45 ± 6
2920A	P2/1	4.32 ± 0.53	4.61 ± 0.61	171 ± 13	150 ± 12	4.47 ± 0.20	161 ± 14
2920B	P2/2	5.78 ± 0.65	6.92 ± 0.93	178 ± 13	133 ± 12	6.35 ± 0.80	156 ± 32
2920C	P2/3	7.26 ± 0.84	6.21 ± 0.70	181 ± 13	182 ± 13	6.73 ± 0.75	182 ± 9
2920D	P2/4	3.80 ± 0.50	4.66 ± 0.63	139 ± 12	127 ± 11	4.23 ± 0.60	133 ± 9
2920E	P2/5	3.58 ± 0.51	4.61 ± 0.67	145 ± 12	137 ± 12	4.10 ± 0.73	141 ± 6
2920F	P2/6	4.54 ± 0.59	4.15 ± 0.55	138 ± 12	134 ± 12	4.35 ± 0.28	136 ± 3
2920G	P2/7	5.04 ± 0.55		221 ± 15		5.04 ± 0.55	221 ± 15
2920H	P2/8	8.09 ± 1.12	5.74 ± 0.76	116 ± 11	134 ± 12	6.91 ± 1.67	125 ± 13
2920I	P2/9	2.67 ± 0.28	4.08 ± 0.34	227 ± 15	434 ± 21	3.37 ± 1.00	331 ± 146
2920J	P2/10	3.98 ± 0.48		161 ± 13		3.98 ± 0.48	161 ± 13
2920K	P2/11	6.85 ± 0.85		140 ± 12		6.85 ± 0.85	140 ± 12
2913A	P3/1	5.68 ± 1.68	4.96 ± 1.61	59 ± 8	43 ± 7	5.32 ± 0.36	51 ± 8
2913B	P3/2	2.49 ± 0.77	1.69 ± 0.55	43 ± 7	45 ± 7	2.09 ± 0.40	44 ± 1

Table SA.4 *(cont.).*

SUTL no.	Field ID	Stored dose / Gy		Sensitivity / photon counts Gy^{-1}		/ Gy	/ photon counts Gy^{-1}
		Aliquot 1	Aliquot 2	Aliquot 1	Aliquot 2	Mean	
2913C	P3/3	2.01 ± 0.66	5.74 ± 2.07	42 ± 6	22 ± 5	3.87 ± 1.86	32 ± 10
2913D	P3/4	1.88 ± 0.79	2.55 ± 0.90	23 ± 5	25 ± 5	2.22 ± 0.33	24 ± 1
2913E	P3/5	1.25 ± 0.45	2.97 ± 0.80	42 ± 6	35 ± 6	2.11 ± 0.86	38 ± 3
2913F	P3/6	1.07 ± 0.42	2.44 ± 0.58	41 ± 6	41 ± 6	1.76 ± 0.69	41 ± 5
2913G	P3/7	3.27 ± 0.99	6.75 ± 2.13	44 ± 7	26 ± 5	5.01 ± 1.74	35 ± 9
2913H	P3/8	4.40 ± 1.87	4.65 ± 1.16	19 ± 4	43 ± 7	4.52 ± 1.29	31 ± 12
2913I	P3/9	7.47 ± 1.36	8.89 ± 1.74	112 ± 11	55 ± 7	8.18 ± 0.71	84 ± 29
2913J	P3/10	12.41 ± 2.12	9.11 ± 1.74	183 ± 14	62 ± 8	10.76 ± 1.65	122 ± 60
2929A	P5/1	3.12 ± 0.38	4.47 ± 0.51	188 ± 14	195 ± 14	3.79 ± 0.95	191 ± 5
2929B	P5/2	4.05 ± 0.54	4.29 ± 0.59	136 ± 12	128 ± 11	4.17 ± 0.17	132 ± 6
2929C	P5/3	4.94 ± 0.70	6.07 ± 0.83	132 ± 12	122 ± 11	5.51 ± 0.80	127 ± 7
2929D	P5/4	4.13 ± 0.51	4.99 ± 0.70	162 ± 13	135 ± 12	4.56 ± 0.61	148 ± 19
2928A	P6/1	9.65 ± 1.19	9.72 ± 0.79	263 ± 16	427 ± 21	9.69 ± 0.87	345 ± 82
2928B	P6/2	8.55 ± 0.86	14.55 ± 0.86	340 ± 18	151 ± 12	11.55 ± 3.00	245 ± 94
2928C	P6/3	19.88 ± 1.56	9.45 ± 1.13	510 ± 23	199 ± 14	14.66 ± 5.21	355 ± 156
2928D	P6/4	17.96 ± 2.82	11.37 ± 3.94	145 ± 12	44 ± 7	14.67 ± 3.30	95 ± 50
2928E	P6/5	12.19 ± 1.35	10.50 ± 0.98	298 ± 17	339 ± 18	11.35 ± 0.85	318 ± 20
2928F	P6/6	2.49 ± 0.58	7.59 ± 1.64	44 ± 8	72 ± 8	5.04 ± 2.55	58 ± 14
2931A	P7/1	8.30 ± 0.91	8.54 ± 0.94	281 ± 17	310 ± 18	8.42 ± 0.77	296 ± 15
2931B	P7/2	9.08 ± 0.39	4.45 ± 0.43	1474 ± 38	356 ± 19	6.76 ± 2.32	915 ± 559
2931C	P7/3	3.27 ± 0.21	1.34 ± 0.18	805 ± 28	285 ± 17	2.31 ± 0.96	545 ± 260
2931D	P7/4	16.61 ± 1.04	13.72 ± 1.81	668 ± 26	159 ± 13	15.17 ± 1.45	413 ± 255

Table SA.5. *IRSL screening measurements on three aliquots of 90–250 μm 15% HF-etched 'polymineral' for SUTL2924.*

SUTL no.	Field ID	Stored dose / Gy			Sensitivity / photon counts Gy^{-1}			/ Gy	/ photon counts Gy^{-1}
		Aliquot 1	Aliquot 2	Aliquot 3	Aliquot 1	Aliquot 2	Aliquot 3	Mean	
2924A	P4/1	7.69 ± 0.88	1.04 ± 0.11	4.89 ± 0.54	60 ± 8	179 ± 13	66 ± 8	4.54 ± 3.32	102 ± 59
2924B	P4/2	4.69 ± 0.29	4.46 ± 0.36	3.70 ± 0.49	124 ± 11	74 ± 9	42 ± 7	4.28 ± 0.49	80 ± 41
2924C	P4/3	7.00 ± 0.35	2.28 ± 0.47	1.65 ± 0.31	141 ± 12	25 ± 5	29 ± 5	3.64 ± 2.68	65 ± 58
2924D	P4/4	7.76 ± 0.83	6.72 ± 0.60	2.85 ± 0.33	49 ± 7	60 ± 8	47 ± 7	5.78 ± 2.45	52 ± 6
2924E	P4/5	5.20 ± 0.39	4.66 ± 0.48	4.43 ± 0.47	78 ± 9	54 ± 7	54 ± 7	4.76 ± 0.39	62 ± 12
2924F	P4/6	6.38 ± 0.44	5.74 ± 0.67	5.10 ± 0.38	90 ± 10	46 ± 7	82 ± 9	5.74 ± 0.64	73 ± 22
2924G	P4/7	10.84 ± 0.49	9.87 ± 0.55	5.86 ± 0.68	163 ± 13	82 ± 9	163 ± 13	8.86 ± 2.49	136 ± 41
2924H	P4/8	12.01 ± 0.58	4.44 ± 1.02	11.84 ± 0.58	149 ± 12	21 ± 5	139 ± 12	9.43 ± 3.79	103 ± 64
2924I	P4/9	7.85 ± 0.52	10.28 ± 0.61	11.26 ± 0.31	92 ± 10	109 ± 10	379 ± 19	9.80 ± 1.70	193 ± 144
2924J	P4/10	6.16 ± 0.52	8.77 ± 0.42	7.40 ± 0.72	64 ± 8	149 ± 12	54 ± 7	7.44 ± 1.30	89 ± 47
2924K	P4/11	10.86 ± 0.57	12.04 ± 0.74	10.71 ± 0.53	132 ± 11	106 ± 10	140 ± 12	11.20 ± 0.67	126 ± 17
2924L	P4/12	8.98 ± 0.99	4.26 ± 0.40	6.29 ± 0.41	46 ± 7	59 ± 8	46 ± 7	6.51 ± 2.36	50 ± 6
2924M	P4/13	9.90 ± 0.80	7.08 ± 0.88	6.95 ± 0.66	67 ± 8	39 ± 6	58 ± 8	7.97 ± 1.48	55 ± 14
2924N	P4/14	14.74 ± 0.91	5.71 ± 0.54	1.91 ± 0.43	101 ± 10	58 ± 8	21 ± 5	7.45 ± 6.41	60 ± 40
2924O	P4/15	11.86 ± 0.97	4.17 ± 0.27	11.24 ± 0.43	68 ± 8	98 ± 10	204 ± 14	9.09 ± 3.85	123 ± 68

Appendix 2 – Supplement B

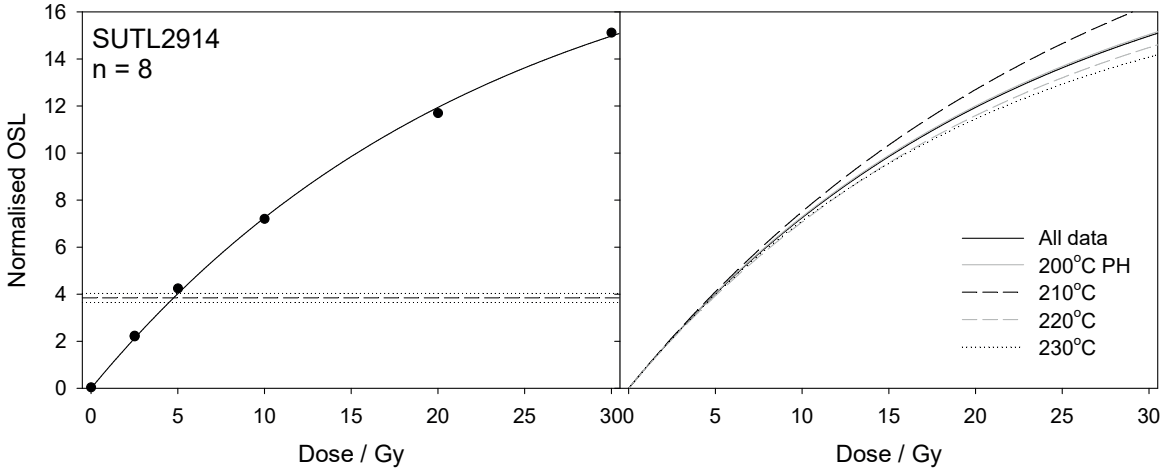

Figure SB.1. *Dose response curves for SUTL2914, showing the mean of all groups (left) with the fitted saturating exponential function and mean normalized natural signal, and the exponential functions for the different preheat groups (right).*

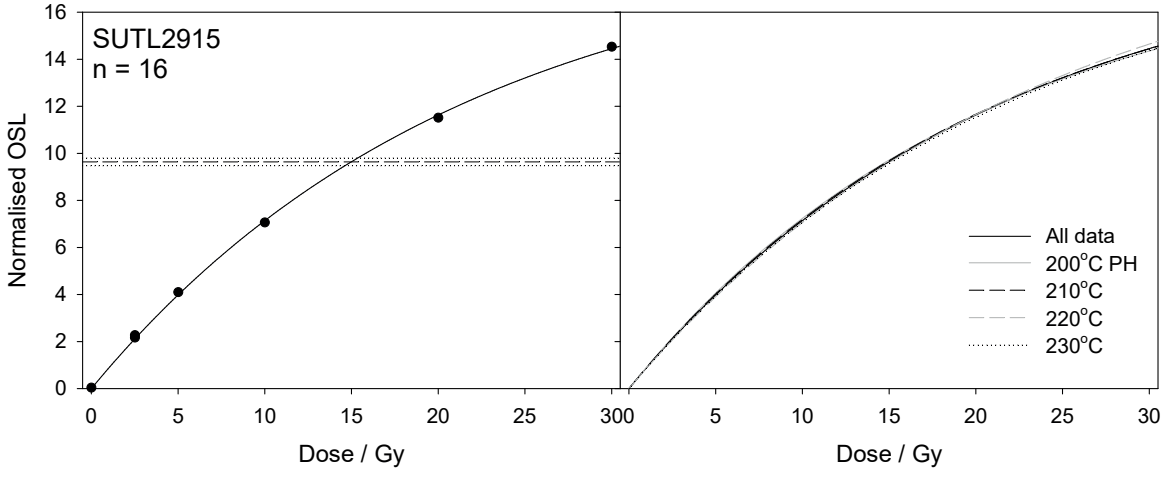

Figure SB.2. *Dose response curves for SUTL2915, showing the mean of all groups (left) with the fitted saturating exponential function and mean normalized natural signal, and the exponential functions for the different preheat groups (right).*

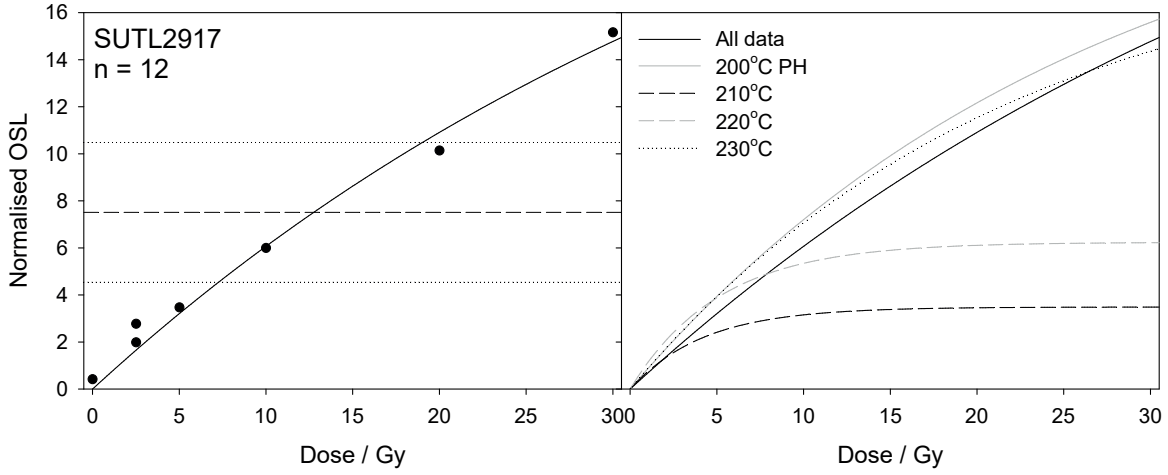

Figure SB.3. *Dose response curves for SUTL2917, showing the mean of all groups (left) with the fitted saturating exponential function and mean normalized natural signal, and the exponential functions for the different preheat groups (right).*

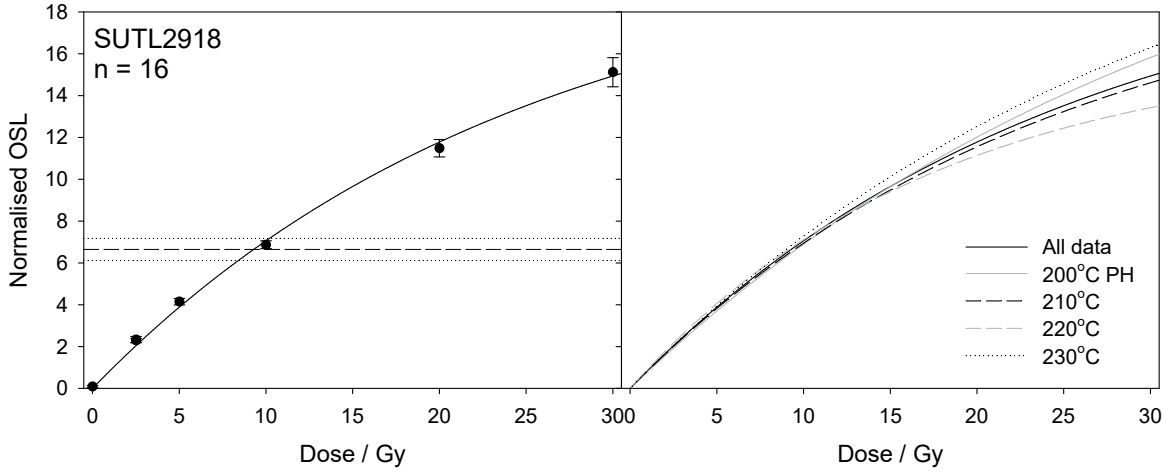

Figure SB.4. *Dose response curves for SUTL2918, showing the mean of all groups (left) with the fitted saturating exponential function and mean normalized natural signal, and the exponential functions for the different preheat groups (right).*

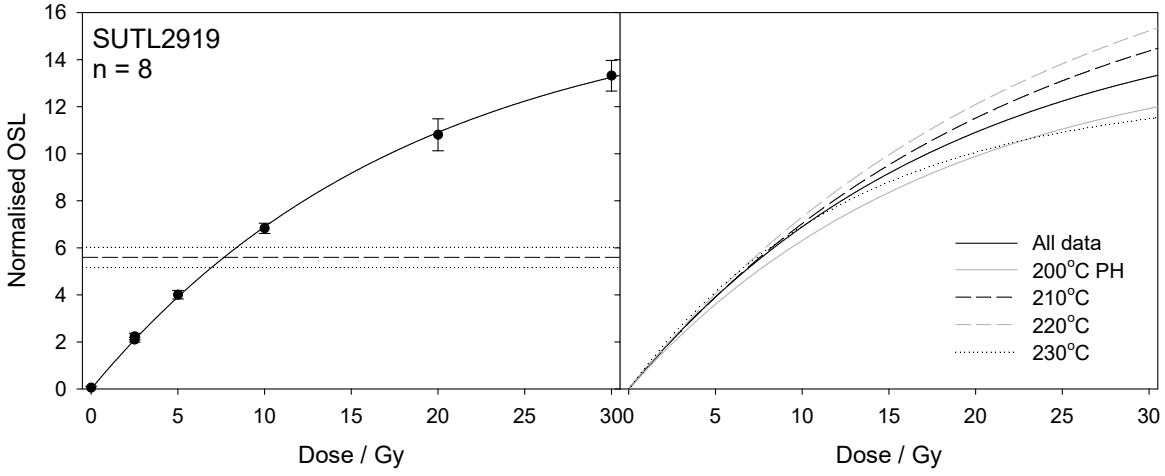

Figure SB.5. *Dose response curves for SUTL2919, showing the mean of all groups (left) with the fitted saturating exponential function and mean normalized natural signal, and the exponential functions for the different preheat groups (right).*

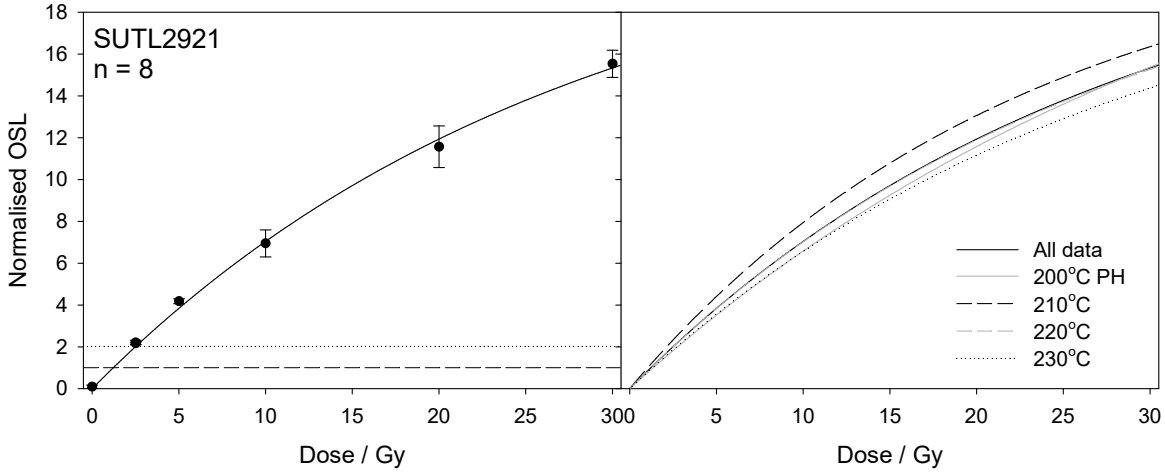

Figure SB.6. *Dose response curves for SUTL2921, showing the mean of all groups (left) with the fitted saturating exponential function and mean normalized natural signal, and the exponential functions for the different preheat groups (right).*

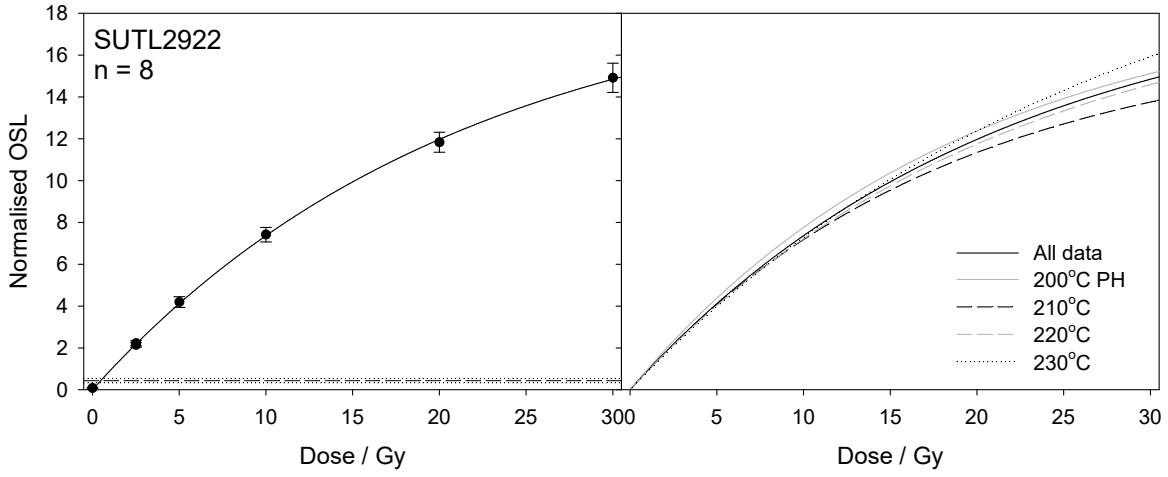

Figure SB.7. *Dose response curves for SUTL2922, showing the mean of all groups (left) with the fitted saturating exponential function and mean normalized natural signal, and the exponential functions for the different preheat groups (right).*

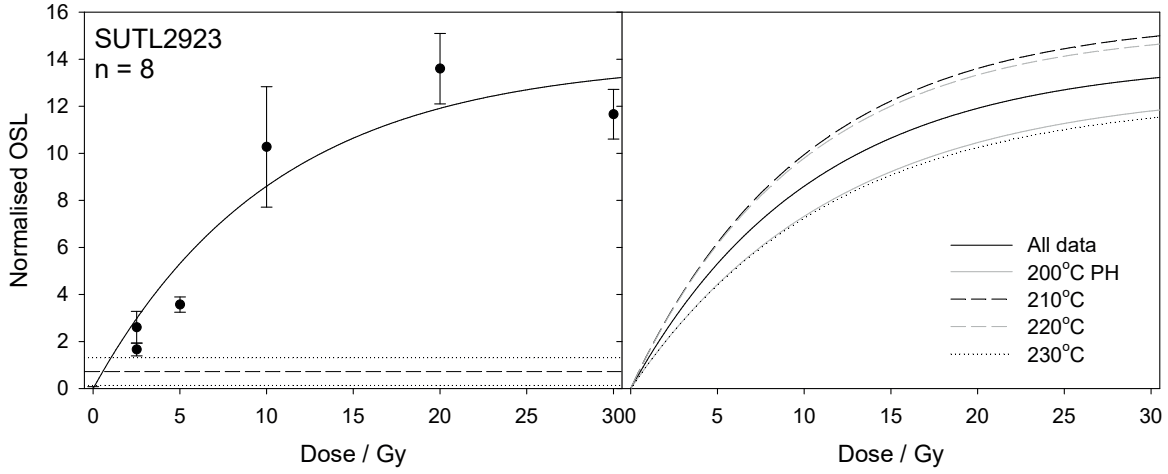

Figure SB.8. *Dose response curves for SUTL2923, showing the mean of all groups (left) with the fitted saturating exponential function and mean normalized natural signal, and the exponential functions for the different preheat groups (right).*

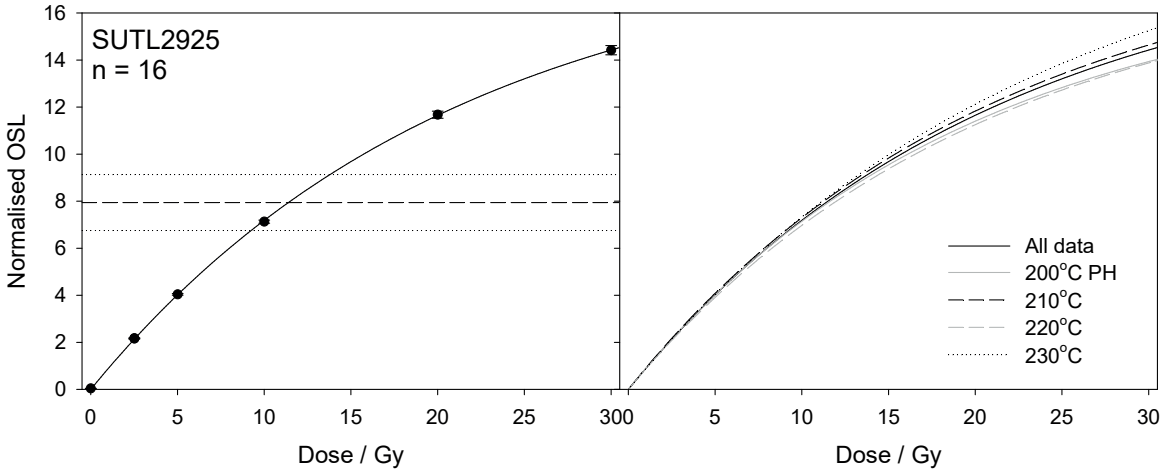

Figure SB.9. *Dose response curves for SUTL2925, showing the mean of all groups (left) with the fitted saturating exponential function and mean normalized natural signal, and the exponential functions for the different preheat groups (right).*

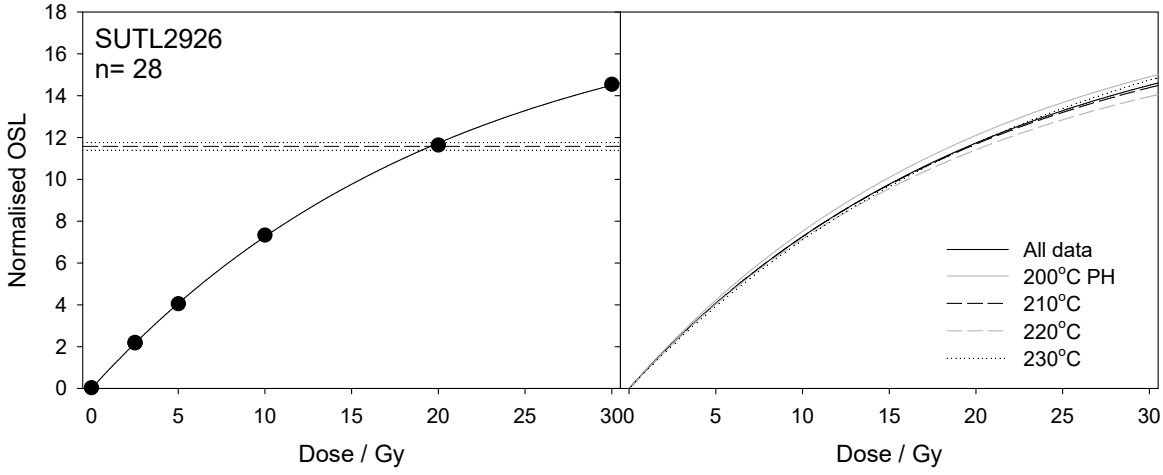

Figure SB.10. *Dose response curves for SUTL2926, showing the mean of all groups (left) with the fitted saturating exponential function and mean normalized natural signal, and the exponential functions for the different preheat groups (right).*

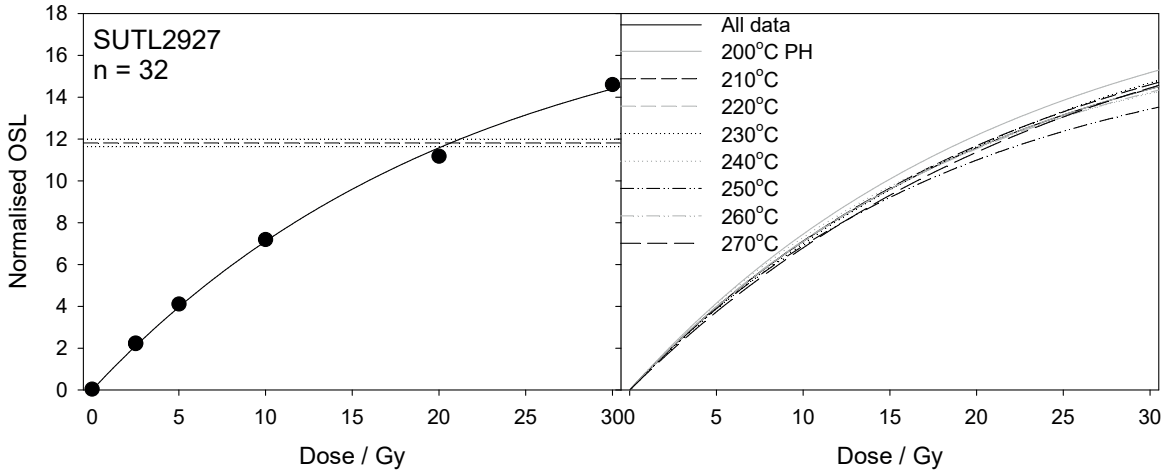

Figure SB.11. *Dose response curves for SUTL2927, showing the mean of all groups (left) with the fitted saturating exponential function and mean normalized natural signal, and the exponential functions for the different preheat groups (right).*

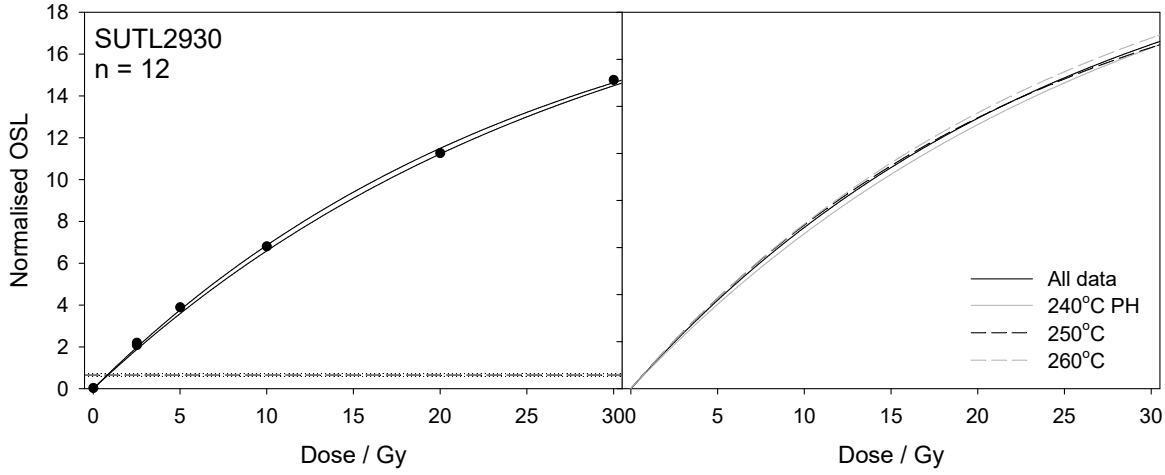

Figure SB.12. *Dose response curves for SUTL2930, showing the mean of all groups (left) with the fitted saturating exponential function and mean normalized natural signal, and the exponential functions for the different preheat groups (right).*

Appendix 2 – Supplement C

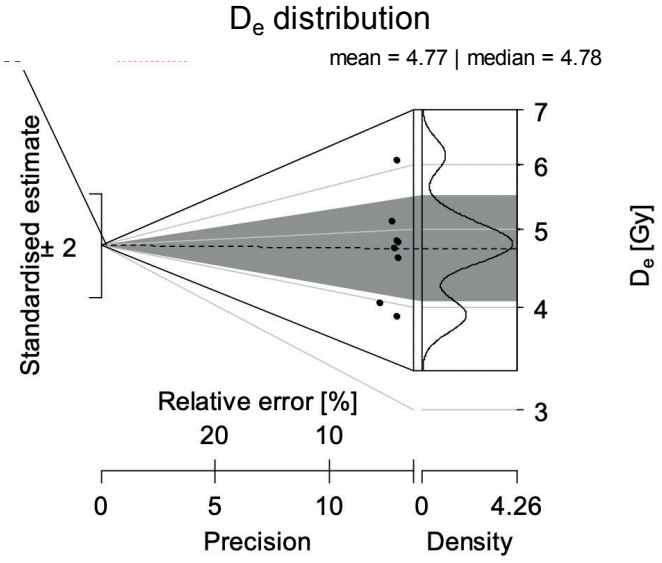

Figure SC.1. *Abanico plot for SUTL2914.*

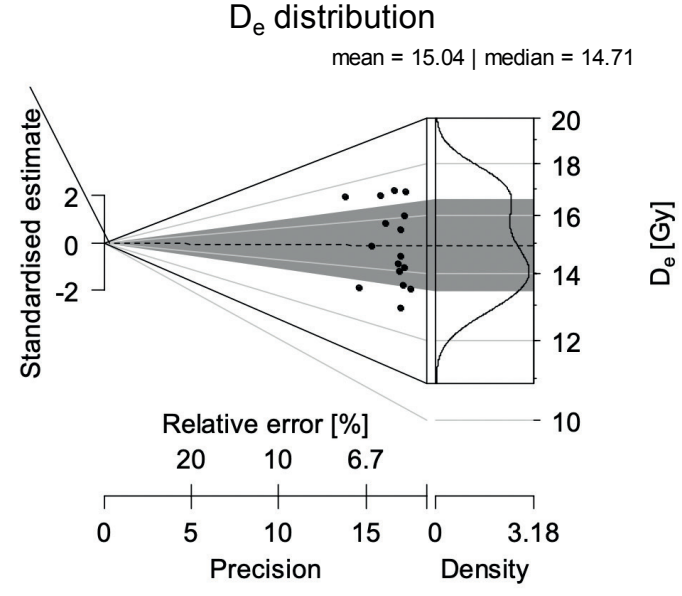

Figure SC.2. *Abanico plot for SUTL2915.*

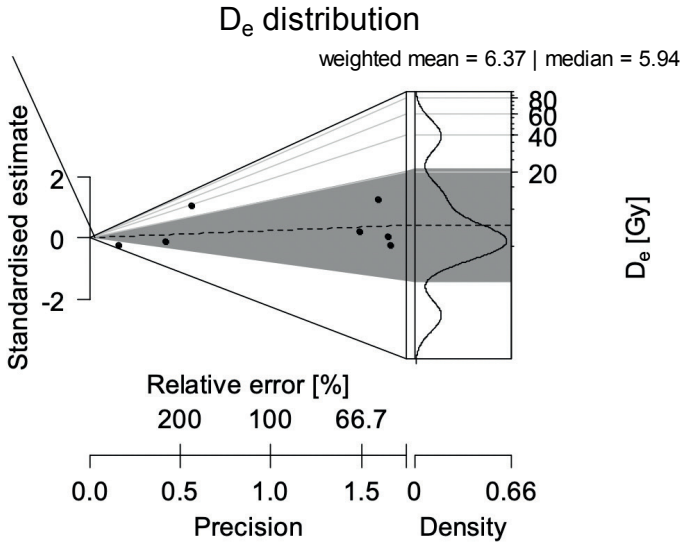

Figure SC.3. *Abanico plot for SUTL2917.*

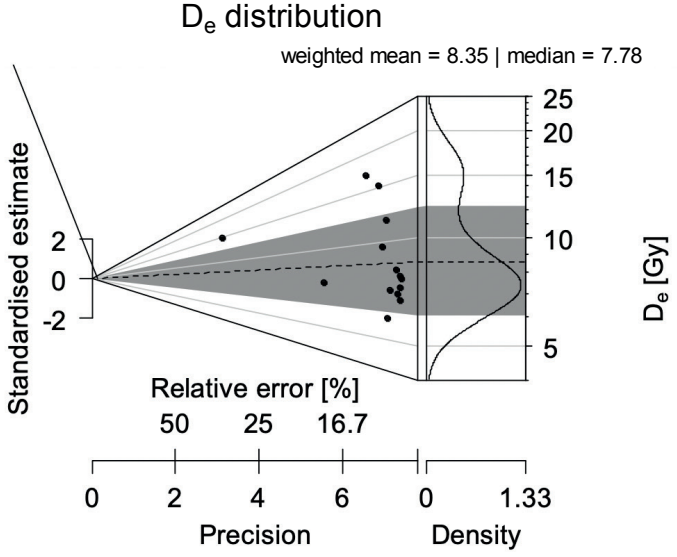

Figure SC.4. *Abanico plot for SUTL2918.*

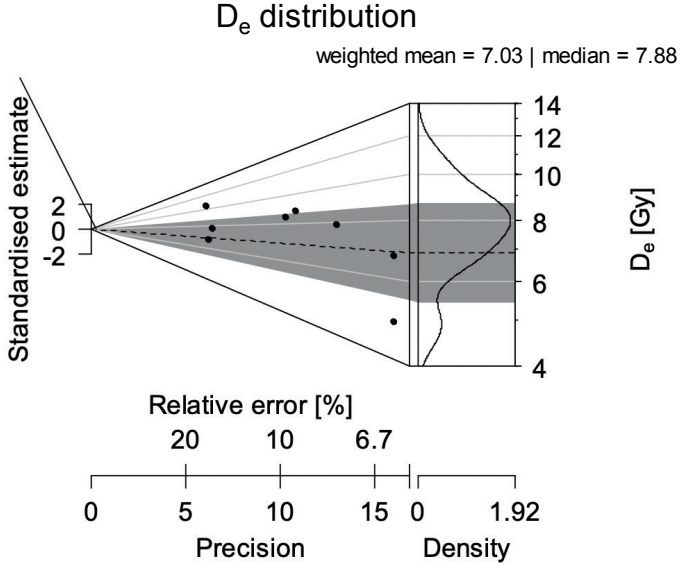

Figure SC.5. *Abanico plot for SUTL2919.*

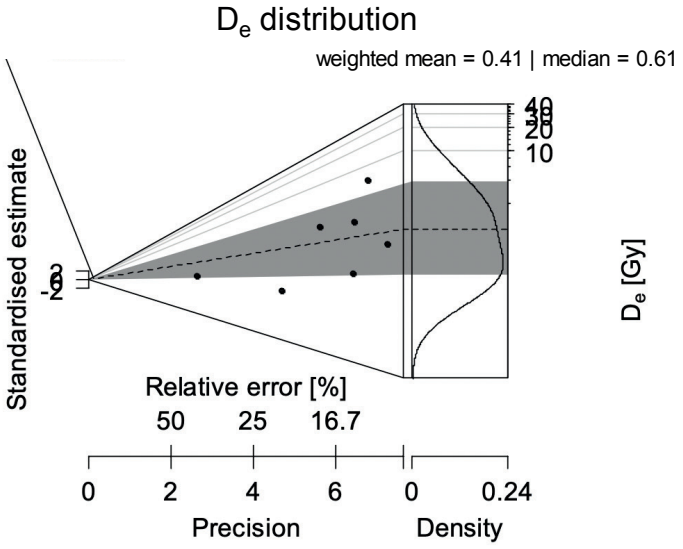

Figure SC.6. *Abanico plot for SUTL2921 (note: data point for -0.032 ± 0.136 Gy excluded).*

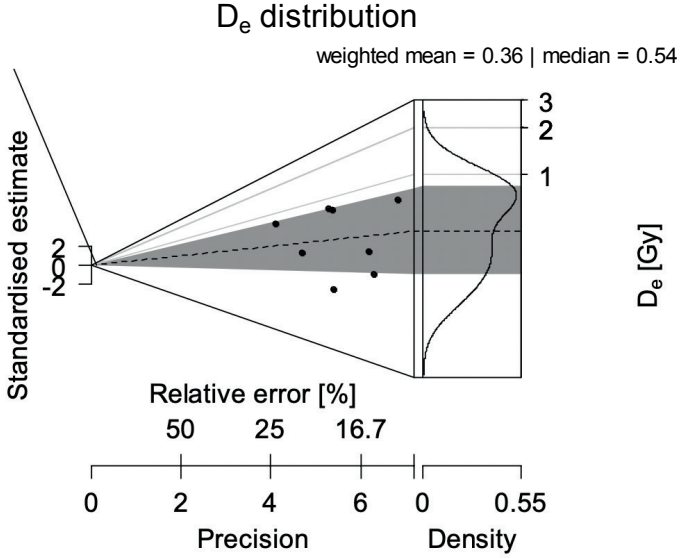

Figure SC.7. *Abanico plot for SUTL2922.*

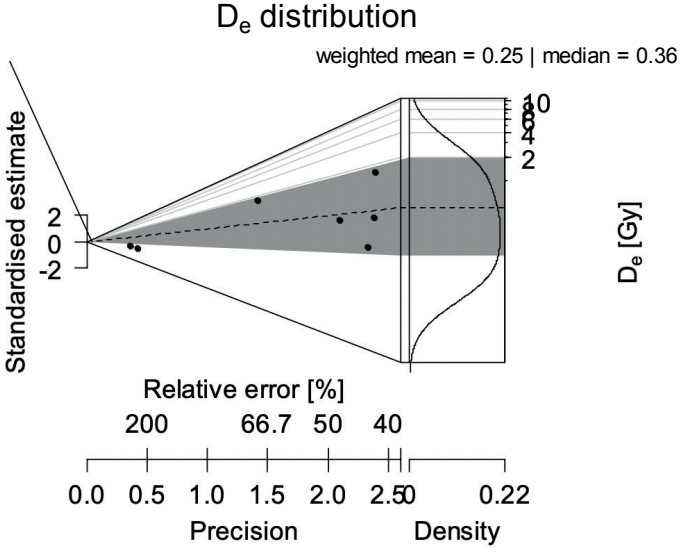

Figure SC.8. *Abanico plot for SUTL2923 (note: data point for -3.03 ± 3.53 Gy excluded).*

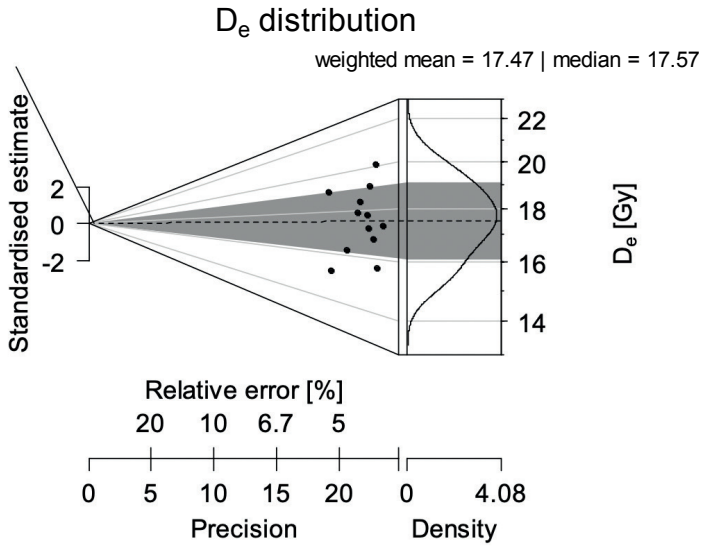

Figure SC.9. *Abanico plot for SUTL2925.*

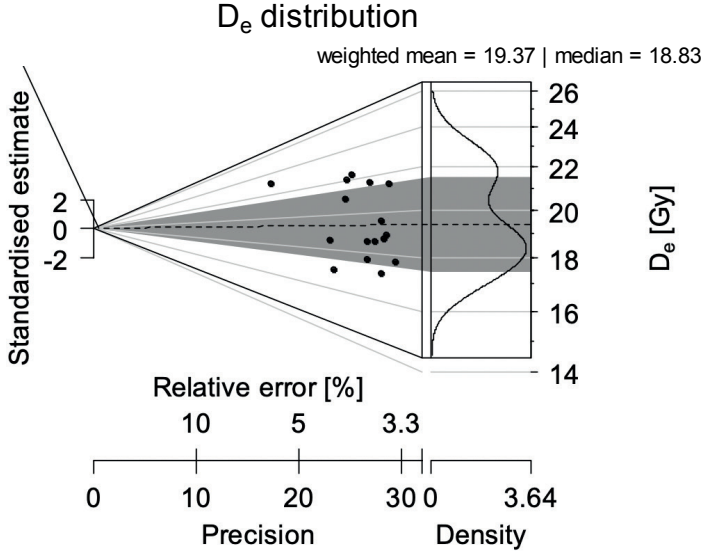

Figure SC.10. *Abanico plot for SUTL2926.*

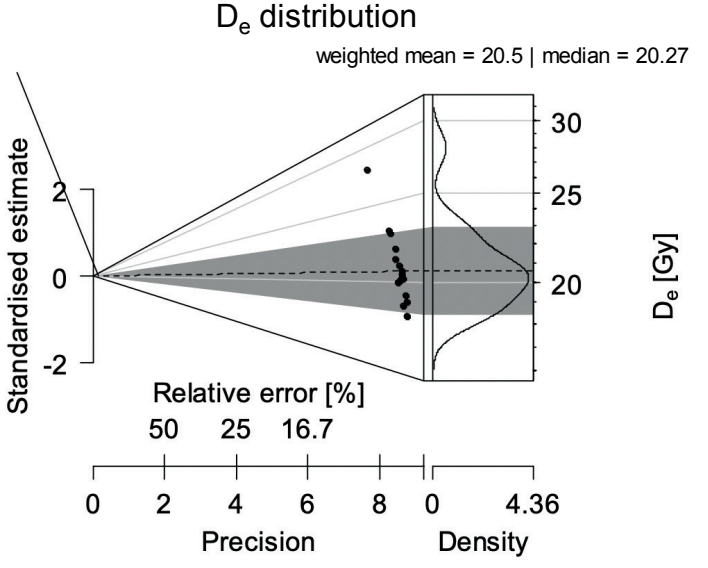

Figure SC.11. *Abanico plot for SUTL2927.*

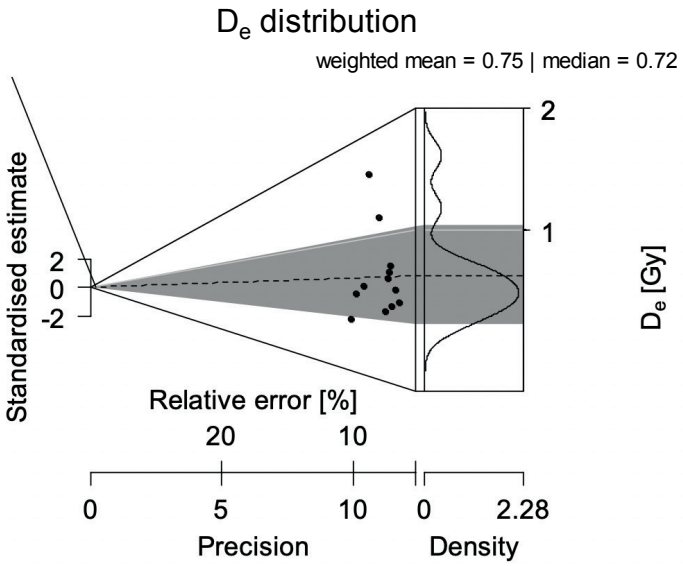

Figure SC.12. *Abanico plot for SUTL2930.*

Appendix 2 – Supplement D

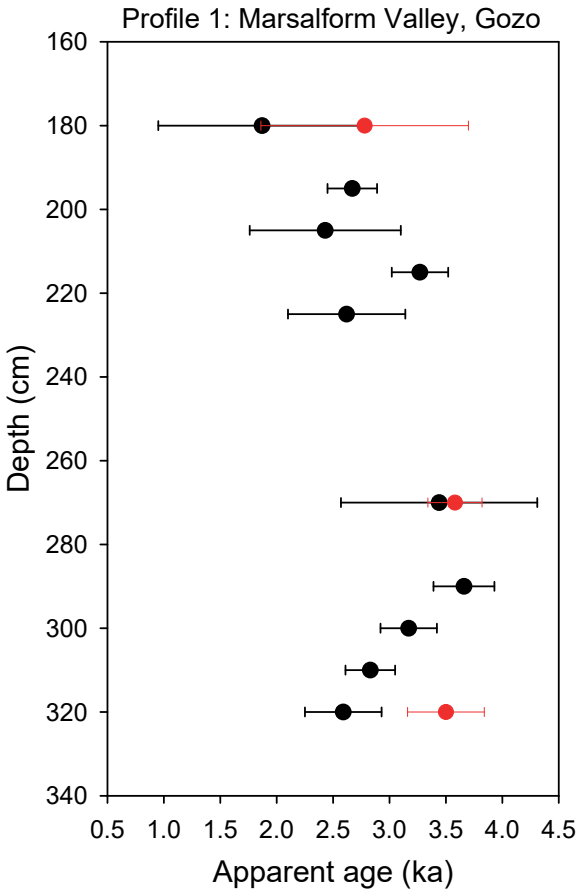

Figure SD.1. *Apparent ages for profile 1 (black) with OSL ages (red).*

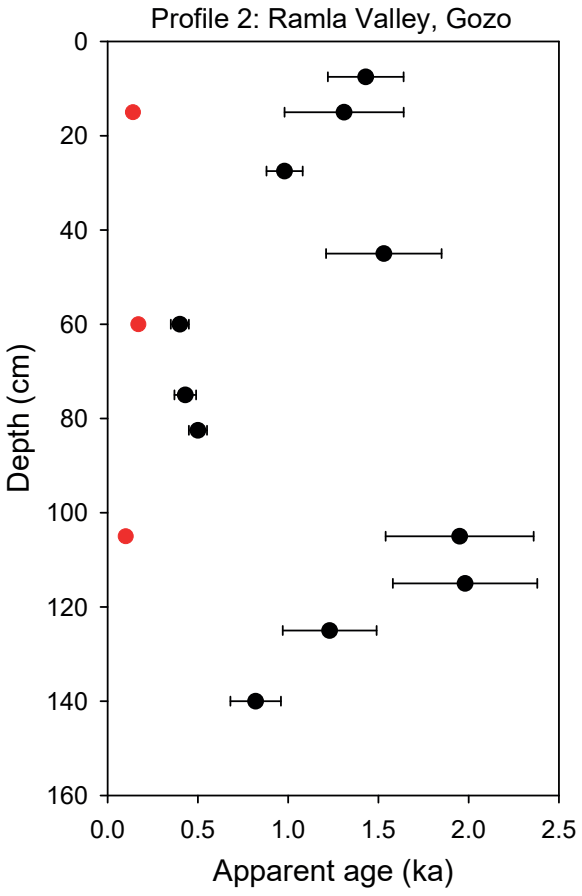

Figure SD.2. *Apparent ages for profile 2 (black) with OSL ages (red).*

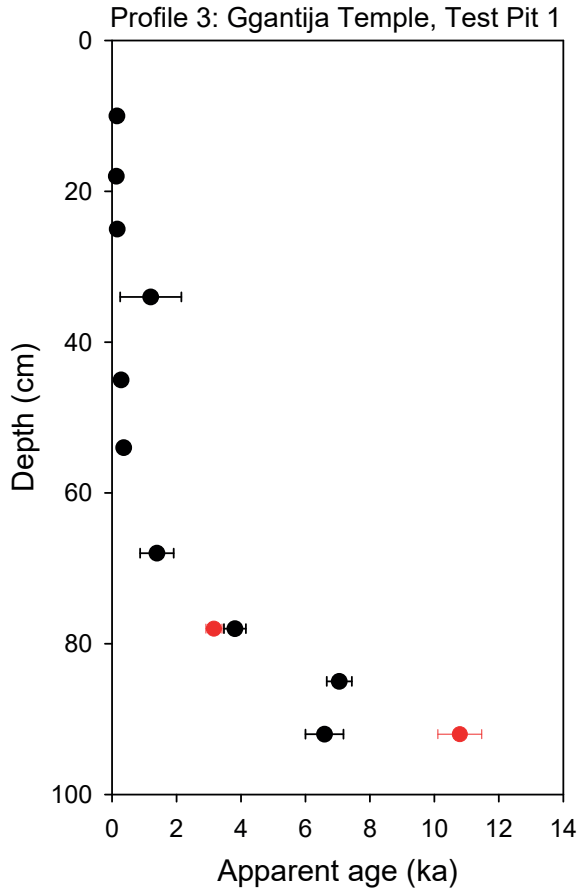

Figure SD.3. *Apparent ages for profile 3 (black) with OSL ages (red). Note that dose rates for 0–75 cm are extrapolated.*

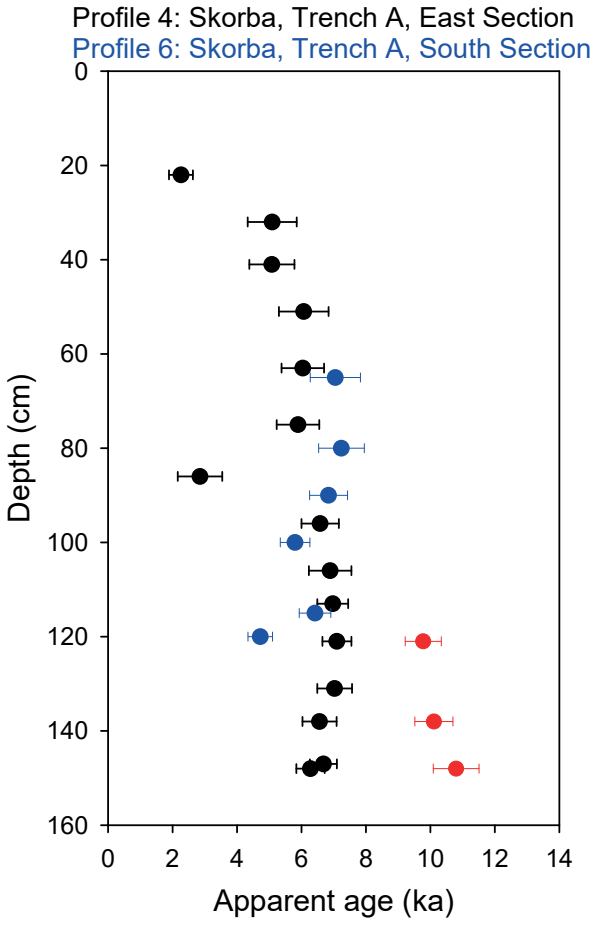

Figure SD.4. *Apparent ages for profiles 4 (black) and 6 (blue) with OSL ages (red). Note that dose rates for 0–120 cm are extrapolated, and for the south section assumed to be the same as the corresponding depth on the east section.*

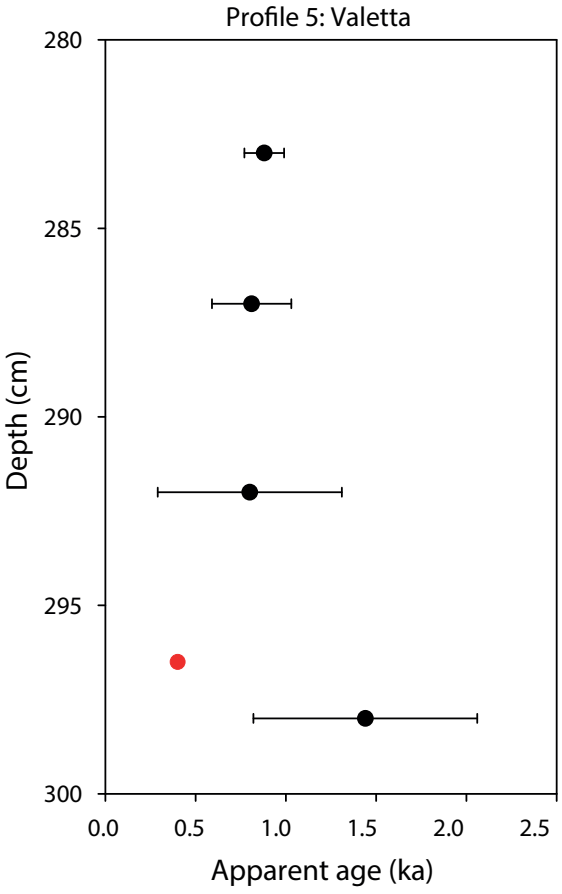

Figure SD.5. *Apparent ages for profile 5 (black) with OSL ages (red).*

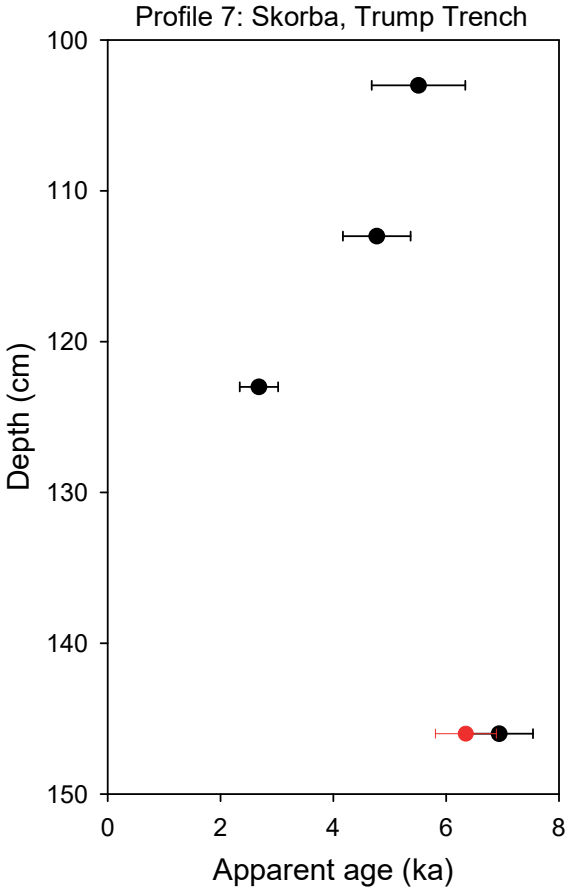

Figure SD.6. *Apparent ages for profile 7 (black). The dose rate for the bottom sample was assumed to equal the corresponding context in P4, the apparent age for that context in P4 is shown (red).*